University of Parma
Department of Physics

-

Study of electrically active defects in structures with InAs Quantum Dots in a GaAs matrix

Mirko Prezioso

Doctorate in Advanced Science and Technology for Innovative Materials

-

XX cycle – January 2008

University of Parma
Department of Physics

-

Study of electrically active defects in structures with InAs Quantum Dots in a GaAs matrix

Doctorate in Advanced Science and Technology for Innovative Materials

Supervisors: Dr. Enos Gombia
Dr. Roberto Mosca

Candidate: Mirko Prezioso

-

XX cycle – January 2008

This PhD thesis has been entirely carried out at IMEM – CNR Institute of Parma and has been supported by the European Network of Excellence SANDiE.

ABSTRACT

In this work, InAs(QD)/GaAs(001) structures are analyzed in order to identify the conditions for plastic strain relaxation via dislocations. To this aim samples with a continuously varying coverage, going from 1.5 to 2.9 ML, have been studied mainly by means of electrical characterization and with the fundamental support of structural TEM analysis, PL measurements and AFM. In the whole coverage range small-sized coherent QDs are formed with diameters and densities that increase up to 15 nm and $2x10^{11}$ cm^{-2}, respectively. At the same time, for coverage above 2.4 ML, large-sized QDs with diameters of 25 nm and densities ranging from $2x10^{8}$ to $1.5x10^{9}$ cm^{-2} coexist with small-sized QDs. We explain the formation of large-sized QDs as the unavoidable consequence of ripening, as predicted for highly lattice-mismatched systems under thermodynamic equilibrium conditions, when the coverage of the epitaxial layer exceeds a critical value. The fraction of ripened islands which plastically relax increases with coverage, leading to the formation of V-shaped defects at the interface between QDs and upper confining layers that propagate toward the surface. The relaxation of those incoherent islands substantially affects the properties of QD structures by (i) reducing the free carrier concentration near the QD plane, (ii) formation of deep levels with typical features related to extended structural defects, and (iii) considerably quenching the QD photoluminescence intensity.

Moreover a preliminary work on Scanning Capacitance Microscopy measurements on these structures have been carried out. The first tests demonstrates a sample ageing due to many hours of ambient atmosphere exposition.

SOMMARIO

FIGURE INDEX

QUANTUM DOTS

A brief history of nanostructures and quantum confinement

One of the basic and most widely used electronic device, nowadays, is the Laser. We can find many lasers operating in our home simply by looking at our CD or DVD players in Hi-fi, TVs or PCs. Another very important laser application is in telecommunications where optical fibres, through which a laser light travels, are the main and most powerful vectors of information.

Laser is an acronym that stands for Light Amplification by Stimulated Emission of Radiation and its basic theory can be traced back to 1917 and Albert Einstein atomic theories, but it was not until 1960 that a laser light was experimented, when T.H. Maiman[1] of Hughes Research Laboratories first achieved laser action at optical frequencies in ruby. Since then, many advances have been achieved and many substances have been used to produce lasers: crystals, liquids, gases and semiconductors. The latter, which is of fairly recent development, offers a lot of advantages in terms of size, reliability and efficiency.

The first semiconductor diode laser was announced by Hall et al.[2] at General Electric Research Labs in Schenectady, New York, in November 1962, very closely followed by Nathan et al.[3] at IBM Watson Research Center in Yorktown Heights, New York, and Quist et al.[4] at MIT's Lincoln Labs in Lexington, Massachusetts. Those three teams demonstrated a laser made from a GaAs diode cooled to liquid nitrogen and pulsed, few micro-seconds, with high current. In a decade this delicate device requiring cryogenic cooling to produce a pulsed light, would become a continuous light, room temperature laser. Nowadays laser devices have no resemblance to the original 1962 structure.

In recent decades, semiconductors research took advantage of the development of growing techniques capable of single atomic layer control and smooth interfaces, to grow smaller and smaller devices. On the road of size shrinking, dimensions soon became comparable to electron de Broglie wavelength, introducing a brand new phenomenon to influence device characteristics: quantum confinement. Starting from the 70s with confinement of carriers in a planar region (one-dimensional well, commonly known as quantum wells), nowadays one of the main direction in

contemporary research is in the production and study of structures with dimensionality less than two: quantum wires, and quantum dots. The latter have been the subject of intense study during the last few years. The strong interest in this structures is the possibility to use them as active media in future high speed electronic and photonic devices. Theoretical predictions[5] of the intrinsic properties of QD lasers include higher characteristic temperature T_0 (which is a measure of the temperature sensitivity of the device) of threshold current (current at which the optical gain is equal to optical loss and lasing starts), higher modulation bandwidth, lower threshold currents and narrower linewidth. In the following pages those theoretical aspects will be briefly introduced.

Quantum confinement advantages for Lasing

As said before, in semiconductors research one of the main instrument used for advances and new scenarios discovery is quantum confinement. In the last 30 years most of the efforts in semiconductors growing techniques were guided from structures engineering in order to find better ways to confine carriers. But why? There is one famous article from Arakawa et al.[6] dated back to 1982 that explains the reasons in a relatively simple manner. In 1982 quantum confinement structures were the quantum wells. By quantum well (QW) is intended, for convention, a 2D-quantum well which means that carriers are confined to live in a plane. QW Lasers were already studied and researchers soon realized that this kind of confinement reduces one of the main problems in lasers: the threshold current density J_{th} temperature dependence. As stated in the Arakawa's article, the improvement in the J_{th} performance can be ascribed to the dimensionality reduction in the free electron motion, from 3D to 2D. As one can expect, increasing confined dimensions would improve the J_{th} behaviour. The reason for such improvement reside in the electron Density of States. The latter, for a bulk (3D), for systems confined in a plane (2D), in a wire (1D) and in a point (0D), is expressed as follow:

$$\rho_c^{3D}(\varepsilon) = \frac{\left(2m_c/\hbar^2\right)^{3/2}}{\left(2\pi^2\right)}\sqrt{\varepsilon},$$

$$\rho_c^{2D}(\varepsilon) = \sum_n \frac{m_c}{\pi\hbar^2 Lz} H\left[\varepsilon - \varepsilon z(n)\right],$$

$$\rho_c^{1D}(\varepsilon) = \sum_{n,l} \frac{\left(m_c/2\hbar^2\right)^{1/2}/(\pi LyLz)}{\left[\varepsilon - \varepsilon y(l) - \varepsilon z(n)\right]^{1/2}}, \qquad (1.1)$$

$$\rho_c^{0D}(\varepsilon) = \sum_{n,l.k} \frac{1}{LzLyLx}\delta\left[\varepsilon - \varepsilon x(k) - \varepsilon y(l) - \varepsilon z(n)\right],$$

Where m_c is the electron effective mass, H is a unit step-like function (similar to the Heaviside function) with $H(\varepsilon \geq 0)=1$ and $H(\varepsilon<0)=0$, Lx Ly and Lz are the lengths of active media and $\varepsilon x(k)$ $\varepsilon y(l)$ $\varepsilon z(n)$ are the quantized energy levels with k,l, and z quantum numbers.

It is important to note that as the confinement is taken into account starting from 2D structures, summation appears and summation indices increase with the number of confined dimensions, reflecting the resulting quantization. As is visible in the Figure 1, the density of states (DOS) is represented by a parabolic function for bulk system, a step-like function for carriers confined in a plane, a multi peaked function in the case of a one dimensional wire and, finally, a collection of delta functions for zero dimensional systems such as quantum dots (QDs).

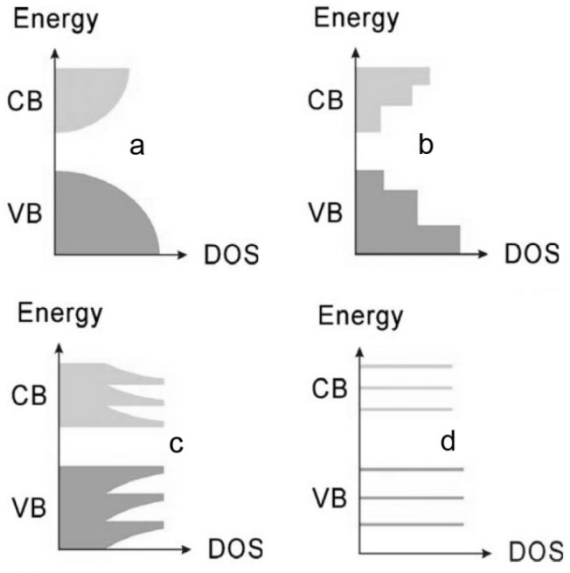

Figure 1 Electron and Holes Density of States for a) bulks, b)Quantum wells, c)quantum wires, d)quantum dots.

A new question arises: why the density of states is so important for *Jth* stability? Starting from the DOS it is possible to calculate the gain of the system and then the threshold current.

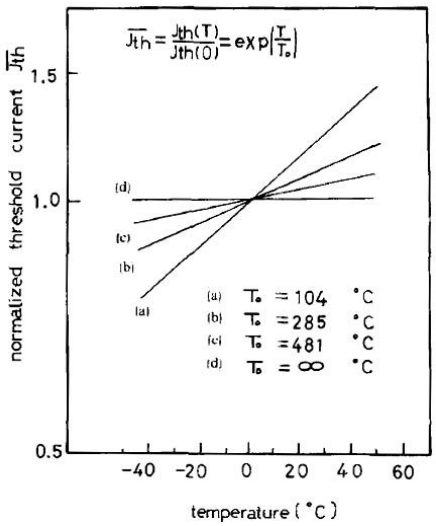

Figure 2 Numerical example of threshold current Jth temperature dependence, normalized by Jth(0). Curves were calculated for a)bulks, b)quantum wells, c)quantum wires and d) quantum dots (Ref. 6)

This is what have been done in Ref. 6 and reported in Figure 2. As we can see the J_{th} temperature dependence is less for more confinement, until it disappears for maximum quantum confinement: in quantum dots. In this figure, J_{th} is normalized for threshold current at T=0°C and expressed as $exp(T/T_0)$. T_0 for different structures is reported in the inset (clearly, the higher T_0 the less temperature dependence).

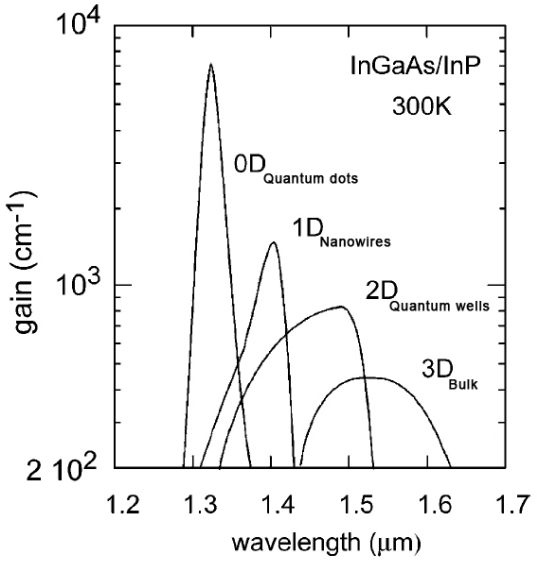

Figure 3 Optical gain for different structures

To understand such a dramatic change of behaviour with temperature, we have to know that J_{th} temperature dependence is ascribed to thermal spreading of injected carriers over a wider energy range of available states, and this leads to a decrease of maximum gain at a fixed injection level.

Consequently, for step-like or peaked DOS functions, such as that of quantum wells and wires, this effect is smaller because of a lack of available states. Instead, in quantum dots, thermal spreading should disappear because the DOS is, ideally, delta-function like.

In Figure 3 gain for all dimensions systems is shown (calculated for comparable structures).

Those curves are calculated starting from the theoretical DOS functions of equation (1.1). It is important to know that the width of quantum dots gain spectrum is determined only by the intraband relaxation broadening since the density-of-states is given by the delta functions, while for other structures it is determined by the shapes of the DOS functions, the intraband relaxation broadening, and the thermal distribution of carriers.

It is clear, from Figure 3 that gain for quantum dots is higher than for other structures. Higher gain means lower threshold current density for lasing, which is another, and one of the most important, advantage of quantum dots lasers. A lower current density needed to start lasing means lower power consumption, lower power dissipation and lower heating which, in turn, extends the device life. For comparison purpose, the first laser generation made from homojunctions had a threshold current density of $5x10^4$ A/cm^2 which could be achieved only with pulses at cryogenic temperatures. A reduction, ~10^3 A/cm^2, can be achieved in structures containing heterostructures, but there is no resemblance to the 20 A/cm^2 which has been accomplished by a QD laser[7]. Moreover, the structure engineering and growing techniques make possible to control quantum dots sizes, strain and other parameters which tunes the laser emission wavelength. This is a key feature in order to tune the QD laser for the windows of interests in photonic applications, such as those for optical fibres communications.

MBE DEPOSITION TECHNIQUE AND SELF-ASSEMBLING

Once the advantage of QDs device has been theoretically established, it is necessary to build such device. Many different methods have been discovered and applied, such as electron beam lithography, nanopatterning and nanolithography, which are all exceptional techniques but with many drawbacks like the lack of instrumentation availability and cost. A more standard, available and cost-effective semiconductor devices growing technique is the epitaxial one. By this term we mean a growth process, atomic layer by atomic layer, with single layer precision, which allows the growth of virtually perfect crystals and interfaces. Although this is a plane by plane 2D growth, under particular condition it is possible to induce a spontaneous three-dimensional growth mode with the formation of self-assembled nano-islands. This process requires the presence of two highly-mismatched materials, one as substrate and the other one growing on it. This growth mode is named Stranski-Krastanow following the names of the two inventors, who theoretically discovered it back in the 1938 but that only in the last 20 years has been implemented. There are many different epitaxial growing methods, but in this case, because the samples were grown by one particular method, we will focus on it: the SS-MBE. This is an acronym that stands for Solid Source Molecular Beam Epitaxy and in this chapter we will briefly see how it works and how the three-dimensional growth mode is achieved.

The MBE machine

The main difference between MBE and other epitaxial method, such as LPE (Liquid Phase Epitaxy) or VPE (Vapour Phase Epitaxy), is the vacuum. MBE is based on the interaction of molecular beams impinging on a crystalline surface under ultrahigh vacuum conditions (UHV). In the Solid Source MBE, those beams are produced by effusion cells which evaporate or sublimate source materials contained in high purity crucibles. There are other types of sources for other variants of MBE, but we will not go deeper into them.

The inside of MBE chamber is maintained at 10^{-11} Torr by a pumping system that consists of cryogenic and ion pumps. Moreover, liquid nitrogen shrouds are present inside the chamber. All these efforts are made in order to reduce contaminants that could be included in the growing crystal during deposition, moreover, to this end, a RGA (Residual Gas Analyzer) is present in the chamber for real-time contaminants concentration control. The ultra high vacuum allows molecules to fly from effusion cells to the substrate without collisions and to be stopped only by shutters positioned at the output of the cells. Those mechanical shutters are electronically controlled in order to allow the growing of the structure previously programmed in the control software. The amount of deposited material is directly proportional to the shutter actuation time (and to the temperature of the crucibles), and this can be as small as it is required to deposit less than an atomic layer. It is important to know that more than one effusion cells can be opened at a time, which means that compound material can be deposited. The result is a machine capable of growing low contaminated crystal (normally 10^{13} cm^{-3} for GaAs) with atomically abrupt interfaces and with controlled composition and doping profile along the growing direction. Those are the basic requirements to grow the new structures needed for new electronic devices.

Going deeper in the SS-MBE chamber description, looking at Figure 4, it is possible to see the effusion cells disposed in front of the rotating sample holder. This is kept at a high controlled temperature in order to activate migration process of adsorbed species on the growing surface.

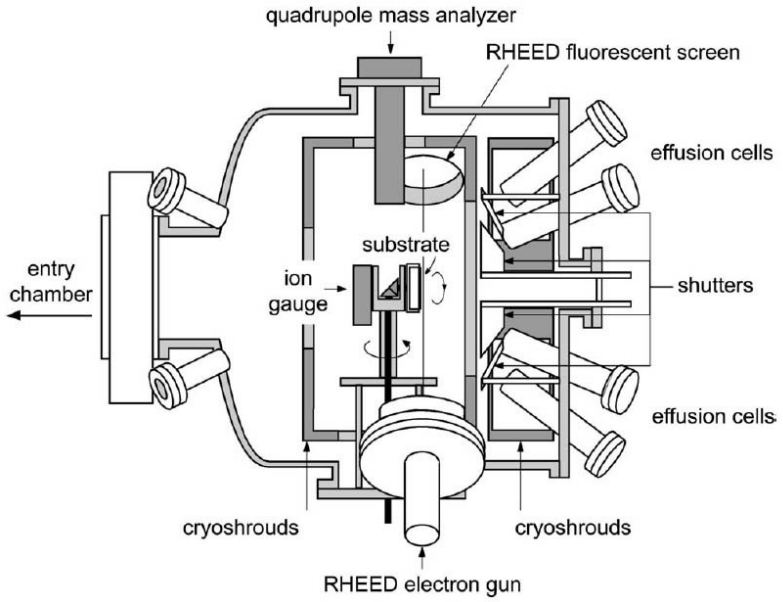

Figure 4 - Schematic of MBE chamber

The sample rotation is used to obtain an isotropic deposition even though the fluxes directions are not perpendicular to the substrate surface. Fluxes are monitored by an ion gauge that can be switched with the sample holder.

Essential to MBE growth process is the RHEED (Reflection High Energy Electron Diffraction) electron gun, used to monitor the single atomic layer coherence, deposition and structure by means of electron diffraction patterns and peaks intensities formed on the fluorescent screen.

Electrons are emitted with an energy in the range of 10-50KeV and impinge on the surface with a glancing angle. This angle is such that electrons do not interfere with the growing surface, but are scattered from surface atoms and structures giving rise to diffraction patterns. Few tens of seconds after the beginning of the surface growth, the diffraction patterns is typical of an atomically flat surface and consists of main strong periodic streaky features with weaker streaks between them. The latter streaks are due to scattering from atoms arranging themselves in a different configuration from the bulk crystal. Different surface structure compared to the bulk one is not surprising if one realizes that surface has a different symmetry with respect to the bulk. Surface growing, technically referred to as “reconstruction”, is an energy minimizing process and so is strongly dependent on the symmetry of the system.

Two-dimensional growth mode

RHEED can be used also in a “time-dependent” mode, in which the peak intensity are related to reconstruction dynamics. At the beginning of growth, at the starting of the entire process or after an interruption, intensity of the zero-order diffracted beam shows pronounced oscillations damping down as the growth proceeds. This behaviour is related to the presence of 2D islands on the growing surface. Assuming that islands are one monolayer (ML) high (the unit cell length in the growing direction), and thus longer than the electrons wavelength, they act as scattering centres reducing the intensities of the peaks positioned in the Bragg directions. Consequently, the steps density is directly correlated to peaks dumping. With this notion in mind, oscillatory behaviour can be explained by the increasing density of steps at the beginning of the growth which reaches a maximum (a minimum in peak intensity) just before islands start to coalesce. Then, the growing process goes on reducing the steps density until the covering of the surface is completed and the minimum step density is reached (maximum in peak intensity). Measuring the period of these oscillations is possible to calculate the time needed for 1ML to be completely deposited.

The growth mechanism which is observed in the oscillatory intensity of RHEED signal is known as layer-by-layer 2D growth mode. Knowing that the incorporation of group-III adatoms (cations) is the most energetically favourable, layer-by-layer 2D mode is the resulting growth dynamics if the surface migration length of such adatoms is shorter than the mean 2D island distance. In this case there would be some cations reaching the low energy site at the edge of growing islands, and others forming new islands on the top of the not yet completed ones (increasing the density of island edges and so dumping RHEED signal). There is a second 2D growth mode, which takes place when the mean diffusion length of cations is longer that the 2D island distance. In this case adatoms reach the preferred site on the island edges causing a lateral growing of such islands. This is known as the step-propagation mode. In this growth mode RHEED signal remains constant.

Cations migration length depends on temperature and on anions population on the growing surface. We know also that anions binding energy is less than cations one, resulting in a higher desorption rate for the firsts. Both facts are exploited in a

special MBE growth process called ALMBE[8] (Atomic Layer MBE). During ALMBE cycles, cations and anions shutters are alternatively opened and closed. While anions shutter is closed, their density on the surface can be reduced because they are preferentially desorbed which means that cations have a longer diffusion length with lower substrate temperature with respect to normal MBE. Another advantage of ALMBE derive from the fact that temperature causes diffusion not only of adatoms on surface, but also of atoms inside the bulk, so maintaining a low temperature reduces the inter-diffusion between grown layers, resulting in sharper composition and doping profiles. We have used this deposition techniques to grow quantum dots and their proximal cap. ALMBE have not been used for the entire sample growth because of its drawback of a high shutter stress which can result in mechanical faults.

Three-Dimensional growth mode

What happens if two lattice-mismatched materials are deposited one on top of the other? For the sake of simplicity, we will refer to the materials used in our samples, InAs on GaAs. These materials have a lattice parameter that differ by 7% (mismatch). This means that at the start of InAs deposition on GaAs, there would be a Layer-by-Layer growing mechanism while InAs adapts the in-plane lattice parameter to that of the GaAs, resulting in a strained layer called Wetting Layer. Within this growing phase, the RHEED shows the streaky pattern. Strain accumulates as the growing proceeds until a critical layer thickness is reached. This thickness depends on the growing conditions and mismatch (the strain source). If we are in the right growing conditions, at this points the RHEED pattern suddenly turns from streaks to spots indicating a brand new symmetry of the growing front. This pattern is the one typical of 3D growing mode. For InAs on GaAs, critical thickness value is 1.6 ML (~0.5 nm). After that this thickness has been reached we have the nucleation of 3D islands few tens of nm wide and few nm high. Such islands, the quantum dots, are homogeneously distributed on the surface. This mechanism of strain relaxation of a layer pseudomorphically (lattice adapted) grown on the underlying epilayer is called Stranski-Krastanow 3D growth-mode[9].

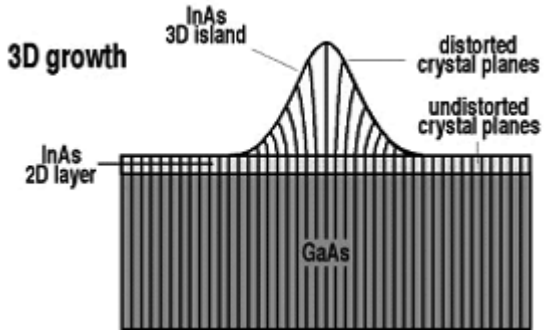

Figure 5 Three dimensional growth scheme. within quantum dots strain is gradually relaxed.

Three dimensional islands formation is not the most natural way to relax accumulated strain. After the critical thickness has been reached, another way in which elastic energy can be released is by dislocations formation. So, why quantum dots are spontaneously formed?

Spontaneous formation of periodically ordered domain structures in solids, with periodicity much larger than lattice parameter, is a general phenomenon, also called self-ordering. This process can occur if an homogeneous system state is thermodynamically unstable and the system undergoes a phase transition into an inhomogeneous state. In this state it is possible to find an order parameter from which a long range field is generated: such a field can be the strain. This means that, in our case, at the critical thickness the homogeneous layer is unstable and a phase transition is occurring. Transition will bring the system to an inhomogeneous state with multi-domains because these can provide compensation to the long-range field: the elastic strain field.

Such self-ordered domains can be of three different types: periodically faceted surfaces, surface domains structures like 2D islands, and arrays of three dimensional coherently strained island when mismatched materials are grown (heteroepitaxy). The latter is our case.

There are three known modes of heteroepitaxy growth: Frank-van der Merwe[10], Volmer-Weber[11], and Stranski-Krastanow[9], the one use in our samples. They represent respectively the layer-by-layer growth, the island growth, and layer-by-layer plus islands growth. The preferred growth mode for a particular system depends on surface and interface energies and on lattice mismatch.

Starting from the case of lattice-matched system, the growth mode is governed only by the interface and surface energies. If the sum of the epilayer surface energy γ_2

and interface energy γ_{12} is lower than the energy of the substrate surface, $\gamma_1+\gamma_{12}<\gamma_1$ the Frank-van der Merwe mode will follows.

A transition in growth mode can occurs if the energies balance is reconsidered in a lattice-mismatched system. In this case we can have an initial layer-by-layer growth due to the low energy of epilayer, but, after few monolayers of deposited material, strain would bring the energy necessary to invert the balance and have $\gamma_1+\gamma_{12}>\gamma_1$, and Stranski-Krastanow growth mode will occurs on the initial *wetting* layer. Experiments of Goldstein[12] et *al*. on InAs/GaAs have demonstrated that these three dimensional island can be *coherently* strained, which means without dislocations formation.

There is a theoretical study[13] in which a comparison of the two competing relaxation mechanism, islands or dislocations formation, is made, and a phase diagram is obtained with dependence on the parameter $\Gamma=\Delta E_{d\text{-}intef}/\Delta E_{surf}$ in where $\Delta E_{d\text{-}intef}$ is the energy relaxed by dislocation of interface, and ΔE_{surf} is the energy that occurs for the formation of islands, which is a positive quantity. If the latter is sufficiently small compared with the former, islands can be formed and the total energy of the island can be written as

$$E_{island} = E_{edges} + \Delta E_{surf} - E^{V}_{relaxation} \tag{1.1}$$

where E_{edges} denotes the short-range energy of islands edges, ΔE_{surf} is the same as above and $E^{V}_{relaxation}$ is the amount of elastic energy of the volume strain that the quantum dots can relax. Now we can look at the scaling behaviour of those terms and see that $E_{edges}\sim L$, $\Delta E_{surf}\sim L^2$ and $E^{V}_{relaxation}\sim L^3$, with L as the island size.

Those scaling factors make possible for the volume term to dominate over the others when it exceeds some critical value. In this condition island formation is energetically favourable.

This means that if we put our samples in the appropriate growth conditions with the right material we are allowed to obtain quantum dots structures without dislocations.

ELECTRICAL INVESTIGATION TECHNIQUES

Introduction to Capacitive methods

One of the most frequently used measurement in electrical characterization is the capacitance of a Schottky barrier or a p-n junction. Studying the behaviour of capacitance of such devices with applied voltage is the basis of many techniques used to investigate the net doping and the electrically active centres by means of their density and profile.

In this work, samples have been prepared with Schottky barrier, so we will concentrate on this kind of device.

When a metal is placed in contact with a semiconductor a Schottky barrier is created. To see how this interface behaves we will make an ideal experiment in the condition that no interface states are present. We start with a metal and a semiconductor not yet in contact. Looking at Figure 6a, the quantity $q\Phi_m$, called work function, is the energy needed to extract an electron from the metal and this is equal to the difference between the Fermi energy of the metal E_{Fm} and the vacuum energy E_0. The work function for the semiconductor is denoted as $q\Phi_s$ and can be expressed as $q(\chi+V_n)$, where χ is the electron affinity, which is a material property equal to the energy difference between the bottom of the conduction band and vacuum, and V_n which represents the distance of the Fermi energy of the semiconductor E_{Fs} from the bottom of the conduction band, dependent on the material doping.

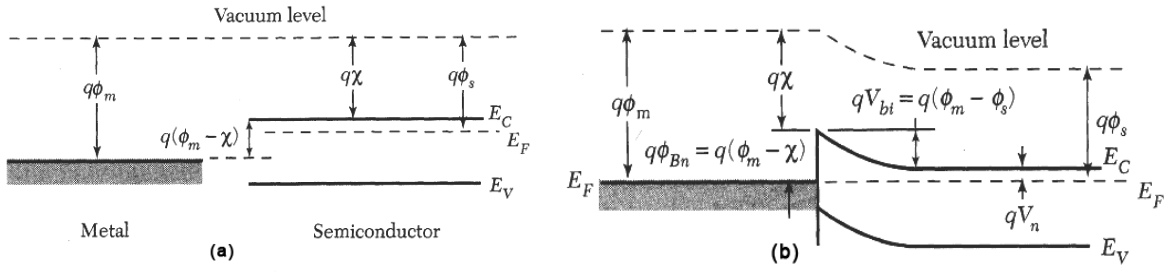

Figure 6 Energy band diagram of metal-semiconductor contacts

If we put the two materials in contact, in the case we have $\Phi_m > \Phi_b$, the semiconductor Fermi level is higher than the metal one and when contact is made between metal and semiconductor this energy difference must disappear to reach the thermal equilibrium. In order to achieve the thermal equilibrium a current of electrons from semiconductor (higher energy) to metal (lower energy) is originated, leaving positive ions in the semiconductor side, forming the so called space charge region, and originating a negative charge on the metal surface. Figure 6b shows the band diagram, after contact is made, resulting from the fact that i) vacuum level is continuous ii) the χ is a material property and iii) Fermi level is constant throughout the system. It is possible to see that bands are bended in the semiconductor side, producing a contact potential equal to:

$$V_{bi} = \phi_m - \chi - V_n \tag{2.1}$$

This is the barrier that an electron would see flowing from the semiconductor to metal side. An opposite flowing electron, from metal to semiconductor, would see a barrier equal to:

$$\phi_b = \phi_m - \chi \tag{2.2}$$

This model is named Schottky-Mott, from the two inventors names.

The theoretical barrier values disagree with the experimental ones because real situation is more complex. One of the most important factor influencing the barrier height is the existence of interfacial states. Indeed, if a large density of surface states is present on the semiconductor surface, the barrier height is independent from the metal work function. This is due to the fact that surface states play the role of a third system with his own Fermi level, and if the density of such states is sufficiently large, they can pin the Fermi level of the semiconductor. Alternatively, when the electric field is produced between metal and semiconductor, if the density of surface states is sufficiently high to accommodate any additional charge produced by this electric field, the semiconductor space charge region would be unaffected and independent from the metal work function.

Lets come back to our ideal Schottky barrier, looking at the band bending: moving away from the metal-semiconductor interface, bands energies return gradually to the bulk values with respect to the Fermi level. As a consequence a potential gradient is

formed, creating an electric field that keeps away semiconductor free electrons and leaves positively ionized donors, forming a fixed positive charge region. The edge of this depletion region is determined by the bands becoming flat which means that the associated electric field is zero. This can be the boundary condition for the Poisson's equation which can be solved, knowing the net charge density, to obtain the electric field and consequently the width x_d of the depletion region. We can briefly look at what happens in the metal. As a consequence of the formation of the semiconductor positive space charge region, electrons accumulates at the metal surface, as a neutralizing negative charge, over a distance x_m into the metal. Due to the much greater metal electron concentration than the semiconductor doping density, we can consider $x_m << x_d$ and assume that the potential across the metal at the contact is negligibly smaller than that in the semiconductor. Those considerations are used in order to resolve the following Poisson's equation.

The electrostatic potential function Ψ is given by

$$\frac{d^2\psi}{dx^2} = \frac{1}{\varepsilon}\rho(x) \tag{2.3}$$

As mentioned before, the bend bending is zero in the bulk away from interface, so, there, $d\psi / dx = 0$, which is a boundary condition. We can now integrate the (2.3) from $x = -\infty$ using the auxiliary variables y and z:

$$\left.\frac{dy}{dx}\right|_y = -\frac{1}{\varepsilon}\int_{-\infty}^{y}\rho(z)\,dz \tag{2.4}$$

and again

$$\psi(x) - \psi(-\infty) = -\frac{1}{\varepsilon}\left[\int_{-\infty}^{x}\left\{\int_{-\infty}^{y}\rho(z)\,dz\right\}dy\right] \tag{2.5}$$

we can integrate by part if we represent the integrand as a product *(uv)* where v=1 and

$$u = \int_{-\infty}^{y}\rho(z)\,dz$$

using the second fundamental theorem of integral calculus which states that given an integral function

$$F(x)=\int_a^x f(t)\,dt$$

its derivative is

$$F'(x)=f(x)$$

we can obtain

$$\psi(x)-\psi(-\infty)=-\frac{1}{\varepsilon}\left[y\int_{-\infty}^{y}\rho(z)\,dz-\int_{-\infty}^{y}y\rho(z)\,dz\right]_{y=x} \tag{2.6}$$

Remembering that at the edge x_d of the depletion layer we have $d\psi/dx=0$ we can then define the integrations limits as $-x_m$ and x_d.

Since the region between $-x_m$ and x_d contains an equal number of positive and negative charge (at equilibrium), the first term of the right end side of equation (2.6) is equal to zero.

If we then define the potential at $x=-\infty$ as zero and describe the band bending relative to it, moreover remembering that $x_m \ll x_d$ such that the lower limit of the integral can be taken to be x=0, then the equation (2.6) gives:

$$V=\psi(x)=\frac{1}{\varepsilon}\int_0^{x_d}x\rho(x)\,dx \tag{2.7}$$

In a uniformly n-type doped material $\rho=eN_d$, where N_d is the doping density, so that the depletion depth becomes:

$$x_d=\left(\frac{2\varepsilon}{eN_d}V\right)^{\frac{1}{2}}. \tag{2.8}$$

Generally speaking, the band bending is the sum of the built-in voltage and the applied bias voltage

$$V=V_{bi}+V_{bias} \tag{2.9}$$

A forward bias is opposite to V_{bi} and its effect is to reduce the overall band bending. In the expression above, we consider a reverse bias as a positive one, and the sign of ρ is consistent with the charges: positive for positive ones. Equations above are

still valid for a Schottky barrier made on p-type semiconductor because the band bending is opposite, just as the accumulated charges, so the sign is restored.

Capacitance – Voltage profiles

Knowing that a depleted region is created under the metal, inside the semiconductor, we can calculate the capacitance associated to it.
The first step is to consider a uniformly n-doped material in which a spatially uniform ionized donors distribution is present inside the depletion region. Considering equations (2.8) and (2.9), we can see that by increasing the V_{bias} of about ΔV, we can increase the depletion width x_d, leaving more donors ionized and so changing the fixed charge per unit area (the diode area) by an amount ΔQ. Using this mechanism, it is possible to define a small signal capacitance C associated with the depletion region:

$$C = A \cdot \lim\left(\frac{\Delta Q}{\Delta V}\right) = A\frac{dQ}{dV} \tag{2.10}$$

where A is the diode area. With this definition, and considering V_{bi} independent from the applied voltage, it is possible to measure C in terms of V_{bias}.
It can be useful to remember that the reason why we are so interested in measuring the capacitance is that from this value we can obtain the net doping density n.
How to extract doping density by capacitance? By knowing the relation between C and n. We need to explicitly calculate the total charge Q inside the depletion region with respect to the band bending V, as stated by equation (2.10). To this end, it is necessary to integrate the Poisson's equation and obtain the electric field. After this, by applying the Gauss theorem it is possible to get the charge $Q(V)$.
Considering the potential to be zero at the edge of depletion layer and that the local carrier density is:

$$n(x) = n_0 \exp\left(\frac{e\psi(x)}{kT}\right) \tag{2.11}$$

where $\Psi(x)$ is the local electrostatic potential, the net space charge is $\rho(x) = e\left(N_d - n(x)\right)$ which can be used in the Poisson's equation to find the electric field as follow:

$$\mathrm{E}^2(x) = \frac{2e}{\varepsilon}\left\{N_d\left[-\psi(x) - \frac{kT}{e}\right] + \frac{kT}{e}N_d \exp\left(\frac{e\psi(x)}{kT}\right)\right\} \tag{2.12}$$

Now we apply the Gauss' Theorem in order to obtain the total space charge Q (per unit area of the diode):

$$\frac{1}{\varepsilon}\int \rho dv = \oint \mathrm{E} dS \tag{2.13}$$

(dv is a volume element and dS is a surface element). We integrate over the whole region to give

$$\frac{1}{\varepsilon} QA = -\mathrm{E}_s A \tag{2.14}$$

Where E_s is the field across the interface between metal and semiconductor, where $x=0$. So, using the root of equation (2.12) into the (2.14), and taking for $\psi(x)$ at $x=0$ the total band bending V, we can obtain the total charge per unit area Q as:

$$Q = \left(2\varepsilon e N_d\right)^{\frac{1}{2}}\left\{V - \frac{kT}{e}\left[1 - \exp\left(-\frac{eV}{kT}\right)\right]\right\}^{\frac{1}{2}} \tag{2.15}$$

Once the total charge Q is obtained, it is differentiated with respect to V and the exact expression of C is gained.

$$C = A\left(\frac{\varepsilon e N_d}{2}\right)^{\frac{1}{2}}\left\{V - \frac{kT}{e}\left[1 - \exp\left(\frac{-eV}{kT}\right)\right]\right\}^{-\frac{1}{2}} \bullet \left\{1 - \exp\left(\frac{-eV}{kT}\right)\right\} \tag{2.16}$$

This expression can be simplified by considering $kT/e << V$ (kT/e at room temperature is 0.025 V while reverse bias is normally more than $\Phi_b \approx 0.7$ V) so that exponential terms can be neglected to give

$$C = A\left(\frac{\varepsilon e N_d}{2}\right)^{\frac{1}{2}}\left(V - \frac{kT}{e}\right)^{\frac{1}{2}} \tag{2.17}$$

Plotting C^{-1} versus the applied reverse bias we can get, for a uniform material, a line with a slope proportional to N_d^{-1} and an intercept of (V_b-kT/e). Indeed, a fundamental consideration, so much used in CV profiles interpretation, is that if a material is compensated by N_a acceptors, the net fixed space charge is $e(N_d-N_a)$ and the slope gives (N_d-N_a) (more detailed discussion will be in while).

What we want is a method for doping profiling, so, after the doping density has been calculated, we need to know the depletion region depth and the form of the potential inside it, or in other words, to which coordinates we can associate the doping value found.

In principle we could integrate the electric field found before in order to obtain the capacitance, and this is exactly what is done, but only after the assumption that

$$\left|\psi(x)\right| >> kT/e \tag{2.18}$$

throughout the depletion region. This approximation, not only simplifies the electric field expression, but also $n(x)$, by the equation (2.11), is affected by means of an abrupt cut-off at $x=x_d$ and a very small, nearly zero, value throughout the depletion region, so that ρ becomes $\rho(x)=eN_d$. With those assumptions, the potential becomes:

$$-\psi(x)=\frac{eN_d}{2\varepsilon}(x_d-x)^2 \tag{2.19}$$

and by putting $-\psi(x)=V$ at $x=0$ we can calculate the total band bending to be

$$V=\frac{eN_d}{2\varepsilon}x_d^2 \tag{2.20}$$

Again, assuming $V>>kT/e$, we can combine equation (2.17) and (2.20) to obtain the practically important, but approximate, result:

$$C=\frac{\varepsilon A}{x_d} \tag{2.21}$$

which is identical to the expression for a capacitor with parallel plates separated by a dielectric material of width x_d and characterized by permittivity ε. This is surprising. The surprise draws from the fact that, unlike conventional capacitors, depletion region contains distributed charges which means that the electric field is not uniform but increases linearly with distance, as can be seen integrating equation (2.19). So it

turns out to be important to distinguish between the capacitance $C=Q/V$ of a parallel plate capacitor and the differential capacitance defined by equation (2.10). In a normal capacitor the charge Q increases linearly with V and the capacitance C is constant and identical to the differential one, while, in the case of depletion region, Q is roughly proportional to $V^{1/2}$ so C cannot be a constant. Even though C is not fixed, we can still define a differential capacitance by considering only small dV, compared to total band bending V, so that dQ can be considered to be varying linearly. In this small signal approximation what we are doing is ignoring all term of order higher than first in the C expansion, which is a normal approximation for small variation around a fixed point.

Another consequence of assuming the approximation expressed by equation (2.18), is that after a small dV has been applied, charge fluctuation occurs only at the edge of depletion region. As we will see, this is not always the case, indeed its wrong when deep states are taken into account. Collectively all the assumptions and simplifications we have made until now are known as "depletion approximation".

It's important to know another consequence of the depletion approximation which gives us quantitatively the measurement limit of this method.

We can use the equation (2.19) and (2.11) to calculate a first order approximation for $n(x)$:

$$\begin{aligned} n(x) &= N_d \exp\left\{\frac{-e^2 N_d}{2\varepsilon kT}(x_d - x)^2\right\} \\ &= N_d \exp\left\{-\frac{1}{2}\left(\frac{x_d - x}{L_D}\right)^2\right\} \end{aligned} \tag{2.22}$$

So that charge density can be written

$$\rho(x) = eN_d\left\{1 - \exp\left[-\frac{1}{2}\left(\frac{x_d - x}{L_D}\right)^2\right]\right\} \tag{2.23}$$

Where L_D is the Debye screening length given by

$$L_D = \left(\frac{\varepsilon kT}{e^2 N_d}\right)^2 . \tag{2.24}$$

Looking at equation (2.22), it is possible to see that free carrier density decreases exponentially with the distance from depletion edge with a rate given by the Debye length.

The demanded requirement of abruptness of depletion edge in the depletion approximation is met when the depletion depth is much bigger than L_D, and even if depth resolution is determined by the step in Δx_d that the instrument can make, Debye length represents the fundamental limit of depletion depth resolution ($\pm L_D$).

Deep states

We now consider the case in which deep states are present in our sample. Indeed, deep states are always present, but in order to influence our measure their concentration N_t must be of the order of (N_d-N_a). We will start with a uniform distribution of deep states as in the Figure 7

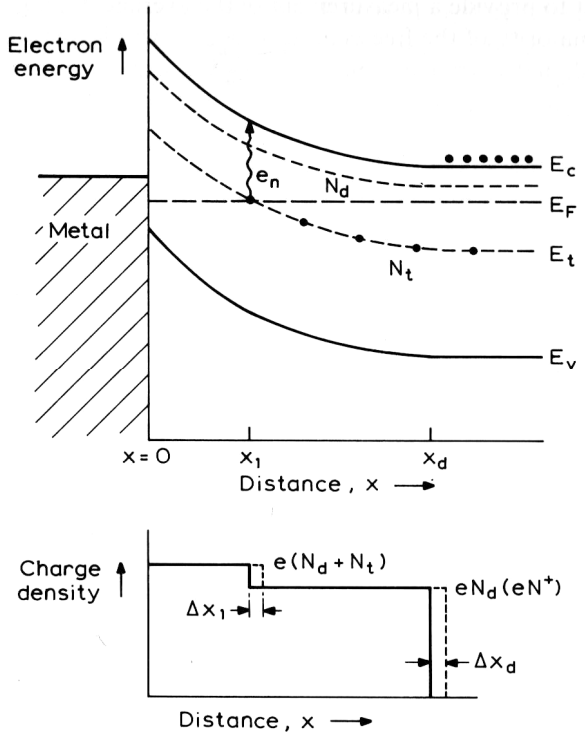

Figure 7 Energy band diagram of a Schottky barrier containing a uniformly distributed deep state with energy level E_t

in which e_n is the emission rate (events per second) of deep states at an energy level of E_t and for a fixed temperature (look at the equation (2.42)). Due to the band bending, the deep states energy level crosses the Fermi level at distance x_1 from the

surface, and for $x>x_1$ all the traps are occupied by electrons. In the region $x_1<x<x_d$ the space charge density is eN_d, while for distances less than x_1 both donors and traps are ionized and the steady state charge density is $e(N_d+N_t)$. The distance x_1 is given by the point at which band bending and separation of the trap level from the Fermi level equals, thus we can write:

$$-e\psi(x) = E_c(x_1) - E_c(x_d) = E_F - E_t \tag{2.25}$$

And using equation (2.19)

$$(x_d - x_1) = \lambda = \left\{ \frac{2\varepsilon}{e^2 N_d} (E_F - E_t) \right\}^{\frac{1}{2}} \tag{2.26}$$

which is independent of reverse bias and x_d. The distance (x_d-x_1) is often referred to as the *transition distance*, □.

So far we have considered the steady state case, but now we will look more deeply what happens when an oscillating voltage is applied. This is important because the capacitance meter uses a resonant circuit in order to obtain the capacitance value, so the voltage is a sinusoidal function with a mean value equal to the reverse bias. What happens while voltage is oscillating? As can be noted in Figure 7, by increasing V by a small ΔV, donors at x_d become ionized and the space charge density is raised by $eN_d\Delta x_d$, but also traps at x_1 are ionized after a time long compared to e_n^{-1} and their contribution $eN_t\Delta x_1$ adds to the space charge. After the small increase, the oscillating bias decreases and the traps in the Debye tail refills, like those at x_1 with electrons at a capture rate named $c_n(x_1)$. It is important to know that since $E_t=E_F$ at x_1, $c_n(x_1)$ is equal to e_n (Ref.14 p. 341) which means that the response of the traps around x_1 is determined by the value of e_n relative to the angular frequency ω_{rf} of the oscillating signal. Only if $e_n>\omega_{rf}$ then the traps can contribute to the total space charge because they have enough time for capture and emission dynamics. Moreover, noting that oscillating voltage modulates only majority carriers, minority traps are not influenced by potential and only acts as static compensating centres if they are acceptor-like.

So, in essence, traps that intercept E_F at x_1 can influence the total space charge depending upon the value of e_n and the modulation frequency.

We will show now this dependence of the depletion capacitance with the frequency, considering the contribution mentioned above (shallow donors, deep donors traps and acceptor levels) on the expression of space charge and, consequently, on the expression of the capacitance.

As we said, shallow donors contribute with a terms equal to $eN_d(x_d)dx_d$, deep donors levels with $eN_t(x_1)dx_1$ and deep acceptor-like traps, negatively charged and acting as compensators, with $-eN_t(x_d)dx_d$ because they are not ionized.

In order to take into account all these contribution, we can express the net uncompensated donor density at the depletion edge $N^+(x_d)$ as:

$$N^+(x_d) = N_d(x_d) - N_a(x_d) + \sum_i N_{ti}^*(x_d) \tag{2.27}$$

N_a represents all the acceptor-like traps with an energy level below the mid gap, and N_{ti} represents the traps above the mid gap and below E_F at the depletion edge x_d. We have used the function N^*_{ti} to represent the different charge state when these traps are occupied, so, depending on their nature:

$N^*_{ti} = 0$ for a donor-like trap

$N^*_{ti} = -N_{ti}(x_d)$ for an acceptor-like trap

We can consider to have a single trap, as shown in Figure 7, and to express the total charge variation dQ at x_1 and at x_d

$$dQ = \int_0^\infty e\delta N(x)\,dx = u(e_n)\,eN_t(x_1)\,dx_1 + eN^+(x_d)\,dx_d \tag{2.28}$$

And, by the use of Poisson equation to relating $\delta N(x)$ to dV

$$dV = \frac{e}{\varepsilon}\int_0^\infty x\delta N(x)dx = \frac{e}{\varepsilon}\left\{u(e_n)\,x_1 N_t(x_1) + x_d N^+(x_d)\,dx_d\right\} \tag{2.29}$$

where

$$\begin{aligned} u(e_n) &= 1 \quad when \quad e_n >> \omega_{rf} \\ u(e_n) &= 0 \quad when \quad e_n << \omega_{rf} \end{aligned} \tag{2.30}$$

If we consider that dx_d is small compared with λ, the space charge integrated between x_1 and x_d remains constant and we can make $dx_1 = dx_d$.

Substituting equations (2.28) and (2.29) into (2.10), we can obtain the capacitance expression as follow:

$$C = \frac{\varepsilon A\left\{u\left(e_n\right)N_t\left(x_1\right)+N^+\left(x_d\right)\right\}}{\left\{u\left(e_n\right)x_1N_t\left(x_1\right)+x_dN^+\left(x_d\right)\right\}} \tag{2.31}$$

and the apparent measured depletion depth is, from equation (2.21),

$$x_{meas} = \frac{u\left(e_n\right)x_1N_t\left(x_1\right)+x_dN^+\left(x_d\right)}{u\left(e_n\right)N_t\left(x_1\right)+N^+\left(x_d\right)}. \tag{2.32}$$

If traps do not respond, which means that $e_n << \omega_{rf}$ and $u(e_n)=0$, the equation (2.31) gives the same value as expression (2.21) and what is measured is called high frequency capacitance C_∞. When, on the contrary, all traps respond, we have $e_n >> \omega_{rf}$ and $u(e_n)=1$ and what we measure is called low frequency capacitance C_0. In this case looking at equation (2.32) we can see that the resulting x_{meas} is different from x_d calculated by the standard equation (2.21). It worth noting that the displacement of x_{meas} from x_d is proportional to the density N_t of the trap. In particular, if $N_t >> N_d$, the value of x_{meas} coincides with x_1.

This should warn us in the interpretation of C-V profiles except in the relative simple cases such as :

1. When $N_t << N^+$ which means that additional contribution to space charge is negligible;
2. When we are using large bias so that $x_1 \approx x_d$ and the fluctuations in charge of shallows and deep levels occurs more or less at the same depth;
3. When the bias is so small that $x_d < \lambda$ which means that deep levels are not ionized due to insufficient band bending.

All this considerations are valid for the oscillating signal, but even if we are using a high frequency, the steady bias is at low enough frequency (practically constant) to let donor traps respond to it.

Deep states start to be ionized at higher enough steady bias values. If $V > (E_F - E_t)/e$, the bias is large enough to ionize the deep states at E_t, moreover, since at this bias the depletion region is large, x_1 is similar to x_d so that, in the case of uniformly distributed trap, we can regard $\rho(x)$ as being composed of $N_d + N_t$ over the whole depletion region.

In the more complex and practical case when N_t is not constant, features in the C-V profile relative to traps positioned at a distance x_t from interface, actually appear at a

depth of $(x_t+\lambda)$. This happens because the instrument indicates a depth of x_d when traps at $(x_d-\lambda)$ contribute to space charge.

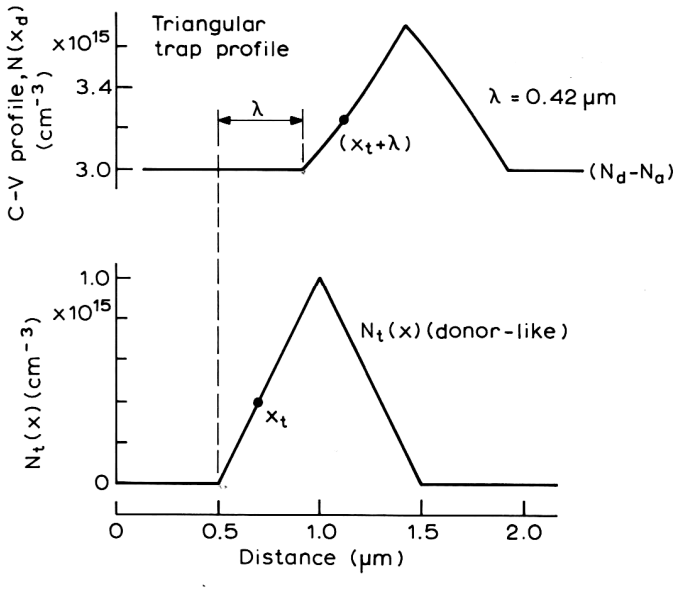

Figure 8 Displacement of a non uniform distribution of deep states. Deep state appear at a distance $x_1+\lambda$.

In the Figure 8 is possible to see the displacement of a triangular distribution of traps. Moreover profile is distorted because of the λ dependence on the free carrier density (see equation (2.26)).

Deep Level Transient Spectroscopy

After C-V profiles have been introduced, it should be clear that they consist of an equilibrium analysis, by which we means that measurements are taken with the sample in thermal equilibrium (it can be a dynamic equilibrium). Many information about deep levels inside the material can be gathered, however, if out of equilibrium time-dependent measurements are taken. We will see now a technique called Deep Level Transient Spectroscopy (DLTS) which take the advantage of this kind of analysis.

We start by considering space charge transients and the rectangular transient charge model, which describes the changing in time of the space charge due to carrier emission from traps.

To be clear we can look at the Figure 9.

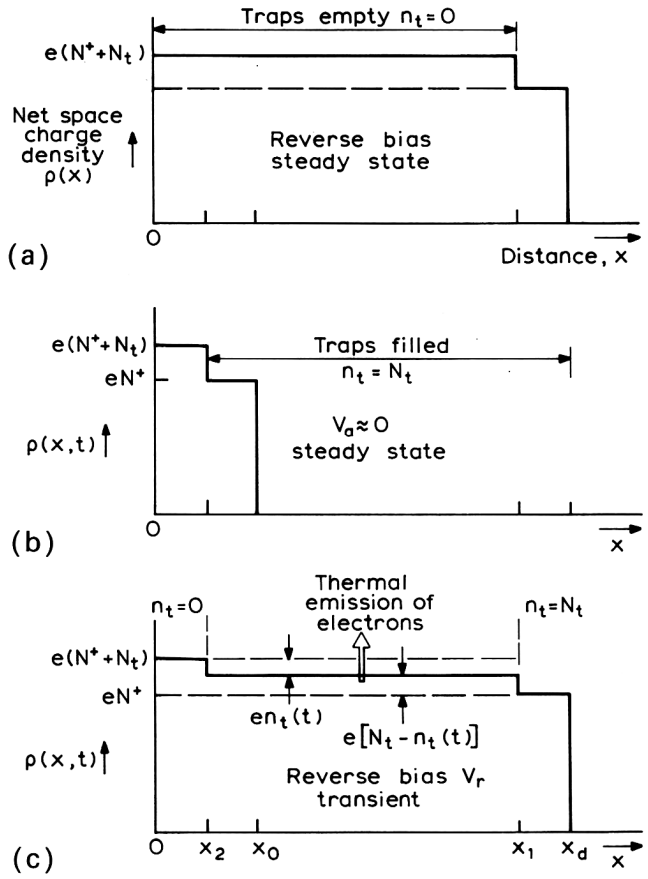

Figure 9 Rectangular transient charge model, a) a steady reverse bias is applied, b) bias is removed or reduced and traps are filled, c) bias is restored and thermal emission of carrier from traps starts.

This illustration shows the rectangular charge transient scheme which is applied in DLTS. Starting from a), here we have the steady state of traps while a reverse bias is applied with traps empty for $x<x_1$ since those traps, because of band bending, are above Fermi level. The second figure b), correspond to the steady state after the reverse bias has been removed or reduced, this phase is called “filling pulse” from the fact that all the traps in the region $x>x_2$ are filled because they return under Fermi level. c) after the filling process the reverse bias is restored and for $x_2<x<x_1$ we have the thermal emission of carrier from traps.

To obtain a mathematical description of those processes (by which it is possible to get traps properties) it is necessary to starts from the beginning and use the Poisson’s equation (2.7). In order to do it, we need the charge distribution $\rho(x)$. This distribution will be time-dependent, and we want it to be, because we are considering out of equilibrium conditions.

The charge profile $\rho(x)$ has three regions:

1. $0<x<x_2$ with traps always empty, such that, calling filled trap concentration n_t, we have $n_t=0$,
2. $x_2<x<x_1$,this is the region where carriers can be refilled by the filling pulse and emitted during reverse bias application. As said before, here n_t is time-dependent,
3. $x_1<x<x_d$ where traps are never empty and remain occupied throughout the cycle. This means n_t is constant and equals N_t

An important assumption is that energy levels, of traps we are considering, are spaced such that only one level relaxes by thermal emission on the time scale of the transient experiment.

Now it is possible to write the charge profile $\rho(x)$ as:

$$\rho(x,t) = e\left\{N^+(x) + \left[N_t(x) - n_t(x,t)\right]\right\} \tag{2.33}$$

Using the expression (2.33) in the Poisson's equation and solve for uniform contribution of N_t and N_d we get

$$V(t) = \frac{e}{2\varepsilon}\left\{N^+ x_d^2(t) + N_t x_1^2(t) - n_t(t)\left[x_1^2(t) - x_2^2\right]\right\} \tag{2.34}$$

Now, looking at the differential of the equation (2.34) with respect to an implicit independent variable (as time is)

$$dV_r = \frac{e}{\varepsilon}\left\{N^+ x_d dx_d + \left[N_t - n_t(t)\right]x_1 dx_1 - \frac{1}{2}\left[x_1^2 - x_2^2\right]dn_t\right\}. \tag{2.35}$$

Results we have so far, are quite general once the rectangular charge transient has been assumed, but now we assume also that voltage V_r is kept constant during the emission cycle which is typical of the more used DLTS method (there is also constant capacitance method but we do not use it in this work). This assumption can be expressed as $dV_r=0$. So we get the time dependence of x_d using (2.35) and derive with respect to time

$$\left\{N^+ x_d + N_t x_1\right\}\frac{dx_d}{dt} - n_t(t)\,x_1\frac{dx_d}{dt} = \frac{1}{2}\left[x_1^2(t) - x_2^2\right]\frac{dn_t}{dt} \tag{2.36}$$

where we posed $dx_1=dx_d$ because with fixed N_d, λ is also fixed (remember that $x_1=x_d-\lambda$). The expression (2.36) is non-linear because as the depletion layer changes its width in response to the changing charge so does the volume investigated and so

(x_1-x_2) also changes. We assume, however, that traps concentration is small compared to the net doping density $N_t<<N_d$ so the moving of x_d is negligible as negligible are also terms of the order N_t. Moreover (x_1-x_2) is constant, so that we can get

$$N_d x_d \frac{dx_d}{dt} = \frac{1}{2}\left(x_1^2 - x_2^2\right)\frac{dn_t}{dt} \tag{2.37}$$

and since $dC/C=-dx_d/x_d$ (from eq. (2.21)) we can calculate the capacitance transient as

$$\frac{1}{C}\frac{dC}{dt} = -\frac{1}{2}\left\{\frac{x_1^2 - x_2^2}{x_d^2}\right\}\frac{1}{N_d}\frac{dn_t}{dt}. \tag{2.38}$$

Considering C effectively as a constant in the limit $N_t<<N_d$, we can calculate the capacitance transient with respect to the steady state capacitance at V_r, that we can call $C(\infty)$ ($t=\infty$,at equilibrium), integrating equation (2.38)

$$\frac{\Delta C(t)}{C} = \frac{C(t)-C(\infty)}{C} = -\frac{1}{2}\left\{\frac{x_1^2 - x_2^2}{x_d^2}\right\}\frac{n_t(t)-n_t(\infty)}{N_d} \tag{2.39}$$

And, knowing that for emission of majority carriers $n_t(t)=N_t exp(-e_n t)$ and that $n_t(\infty)=0$, the equation (2.39) gives

$$\Delta C(t) = -\Delta C_0 \exp\left(-e_n t\right) \tag{2.40}$$

where

$$\frac{\Delta C_0}{C} = -\frac{1}{2}\left\{\frac{x_1^2 - x_2^2}{x_d^2}\right\}\frac{N_t}{N_d}. \tag{2.41}$$

Thus, in the dilute limit ($N_t<<N_d$) the capacitance transient is an exponential with a time constant equal to e_n^{-1} and an amplitude proportional to N_t.

Another fundamental observation is that e_n characterizes the deep level giving us information on its activation energy (proportional to distance from its energy level and the bottom of the conduction band) and its capture cross section. This is true because

$$e_n(T) = \gamma T^2 \sigma \exp\left(-\frac{\Delta E}{kT}\right) \tag{2.42}$$

where

$$\gamma = 2\sqrt{3}M_c \left(2\pi\right)^{\frac{3}{2}} k^2 m^* h^{-3}$$

with M_c as the number of conduction band minima, k, m^* and h as always. σ is capture cross section that directly influences the capturing speed of the level (like in nuclear physics), and ΔE is strictly correlated to the energy level of the trap. Consciousness is required when using those values. ΔE is identified as $(E_c-E_t)+\Delta E_\sigma$ so it does not give energy of the trap directly but it is influenced by energy required for its activation. ΔE is called activation energy.

Now we focus on measuring the time constant of the exponential transient as reported in equation (2.40).

The essence of DLTS method is the measure of $C(t)$ twice during the transient with a predefined time interval representing a preset time constant $\tau_{ref}=e_n^{-1}$, called rate window, and recording the difference. The operating principle is as follow.

We can imaging to test a sample containing two different traps with different values of ΔE and σ. We start by setting the reverse and filling voltages such that the explored volume contains the traps, more precisely they must be within (x_2-x_1) interval. Then we bring the sample at low temperature, usually using NL_2, and start heating slowly towards higher temperatures. As the temperature of the diode is increased the emission rate increases as well and a peak would occurs in the DLTS signal when the rate of emission of traps equals the rate window set on the instrument $\tau=e_n^{-1}=\tau_{ref}$. This would happen two times because we have two traps with different emission rate, so in a graph reporting DLTS signal we would see two peaks, at different temperatures, representing the two levels. For a given τ_{ref} the temperatures of the peaks are characteristic of the levels and the peak amplitude is proportional to ΔC_0 and gives the trap concentration N_t. We can go further, and repeat the scans with different rate windows so to obtain different peaks temperatures for the same trap level. With a set of couples (e_n, T_{peak}) is possible to generate an Arrhenius plot of $ln(e_n^{-1} T^2)$ versus T^{-2} and to get values of ΔE and σ for each trap by fitting the curves. It is possible to work with very short time constants (in the ms range and below) so that with slow heating rate, sampling of the transient is repeated many times with a high gain in the signal-to-noise ratio. With this method resolution of $\Delta C_0/C \approx 10^{-4}$ is possible without specialized instruments.

Extended defects

The detrimental role of defects in general, and of dislocation in particular, in semiconductors materials is known. Many techniques have been developed and used to study such defects (EBIC, CL, PL…etc) but DLTS remains one of the most powerful.

That is true because dislocations are known to introduce deep levels in the band gap due to the dangling bonds in the dislocation core[15], so a Deep Level Spectroscopy technique should see such levels. The issue is that such levels would not be the only levels present, there could be many other levels with different origins (intrinsic point defect, contaminants, quantum confining structures), so how to discern the extended defects levels?

We will now follow the work from T. Wosinski[16] who starts from a recombination via dislocations model of T.Figielski[17] to analyze the electron capture kinetics at linearly arranged traps, like the ones we can find at a dislocation line.

We define N_T as the average trap concentration in the crystal and *f* as the fraction of those traps actually occupied by electrons. Those traps, filled with electrons, generate an electrostatic potential of magnitude Φ around them. Such a potential would be responsible for the Boltzmann term in the expression for the fraction of electrons with sufficient energy to surmount such barrier. The total amount of those electrons would be, starting from *n* as the electron concentration outside the barrier, $n\exp(-q\Phi/kT)$ (we are not considering tunnelling effect).

We can write the rate equation for the capture of electrons at those traps during the filling pulse of duration t_p:

$$\frac{dn_T}{dt_p} = \sigma_n \bar{v}_n n N_T \left[1 - f\left(t_p\right)\right] \exp\left(\frac{-q\Phi\left(t_p\right)}{kT}\right) \tag{2.43}$$

Where $\bar{v}_n$ is the mean thermal velocity of electrons.

Now, from the work of Read[18] we can assume the potential to be linearly dependent from *f* and hence it can be written

$$\Phi\left(t_p\right) = \frac{\Phi_0 n_T\left(t_p\right)}{n_{T0}} \tag{2.44}$$

Where $n_T(t_p) = f(t_p) N_T$ and the suffix 0 indicates an equilibrium value. We can neglect the term *[1-f(t_p)]* in equation (2.43) with respect to the exponential factor and find an approximate solution with the initial condition $n_T(0)=0$

$$n_T(t_p) = \frac{kT}{q}\frac{f_0}{\Phi_0} N_T \ln\frac{t_p+\tau}{\tau} \tag{2.45}$$

If we assume $f<<1$ which means that we never saturate n_T with the duration of filling pulse t_p, the time constant τ can be written as

$$\tau = \frac{\left(\frac{kT}{q}\right)\left(\frac{f_0}{\Phi_0}\right)}{\sigma_n \bar{v}_n n} \tag{2.46}$$

So that by introducing the expression (2.46) in the (2.45), we can obtain the capture kinetics of electrons at the dislocation line to be:

$$n_T(t_p) = \sigma_n \bar{v}_n \tau n N_T \ln\left(\frac{t_p+\tau}{\tau}\right). \tag{2.47}$$

The expression (2.47) gives a logarithmic dependence of n_T, and hence of the connected DLTS peak amplitude, with the filling pulse duration, so giving to DLTS a method to discern if the origin of the peak is due to extended defects.

Scanning Capacitance Microscopy

On the road to nanometric dimensions of electronic devices, new characterization techniques have to be created in order to analyze such devices.
One of these relatively new techniques is the Scanning Capacitance Microscopy (SCM), which combines the advantages of Scanning Probe Microscopy with the features of the electrical capacitance methods.

SCM has been recognized as a leading approach for obtaining two-dimensional dopant profiles of semiconductor devices.

All techniques of the SPM family rely on the interaction of a tip, with a radius typically in the tens of nm range, with the sample (see Figure 11 p. 43). The type of interaction measured establishes the kind of microscopy that is carried out. In the case of SCM, a conducting tip is scanned over the sample surface and small changes in the tip/sample capacitance are recorded.

The capacitance we are interested in, is the one associate to the depletion region created under the tip in the semiconductor. The analogy with a Schottky barrier and its depletion region would be complete if an insulator layer represented by the unavoidable oxide that exist on the semiconductor, would not be present. This additional insulating layer gives to such electrical device the name MOS: Metal-Oxide-Semiconductor. The presence of the oxide changes the C-V curve of such device with respect to the Metal-Semiconductor one (Schottky barrier).

The ability of SCM to measure the electronic properties of the analyzed surface through an insulating layer is in contrast with Scanning Tunneling Microscopy or with Conducting Atomic Force Microscopy, which requires finite conductivity in order to obtain a measurable current. The SCM relies on the displacement current and thus can image materials inaccessible to STM or C-AFM. However the presence of a depletion region require a free carrer density in the range from ~10^{14} to ~10^{20} cm^{-3}.

Basics of MOS C-V characteristics

The theory of the one dimensional MOS capacitor provides a basis for understanding dopant profiling by SCM. Here we would not go deeply in the MOS physics, instead we will only set the basis to understand SCM. For a more detailed analysis let me remind the excellent book from Sze[19].

Like in the case of a Schottky barrier, the MOS capacity is voltage dependent, and this dependence provides the most important information for dopant profiling.

Normally, like in the case of C-V profiling with Schottky barrier, the capacitance voltage dependence is found by measuring the capacitance as a function of the dc bias. The C-V response of a MOS depends dramatically from the AC test signal frequency (Figure 10).

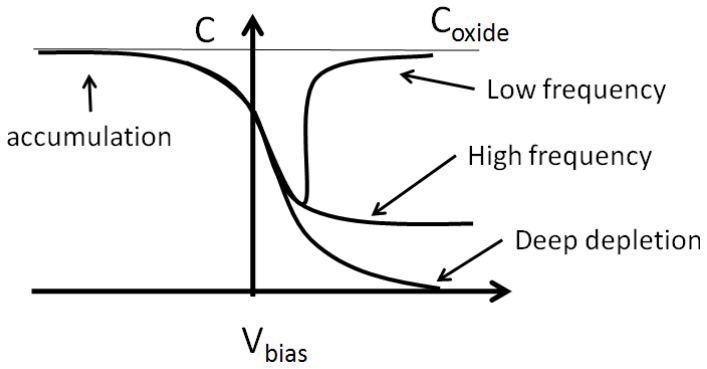

Figure 10 MOS C-V curves at different frequency. In this graph a n-semiconductor is considered, and the metal electrode (tip) is grounded like in the SCM apparatus. (In alternative, the curves are the same for p-type and grounded sample).

For direct biases, the band bending is reduced, the depletion region vanishes, and what we measure is the fixed oxide capacity, this regime is called *accumulation*.

Now going to the reverse biases, increasing the band bending, we expand the depletion region and measure a decreasing capacitance due the series of the oxide capacitance and the space charge capacitance inside the semiconductor. This is exactly what we see in Figure 10 for all test signal frequencies. Increasing further the bias the band bending would make the valence band (we are considering n-type semiconductor) nearer the Fermi level, and, what is called an *inversion* layer, is formed. In the case of low test signal frequency (<100Hz), minority carriers have enough time to respond and, the capacitance at large reverse voltages raises back to the initial value, because the capacitance measured would be the that of the oxide.

On the contrary, if the test signal frequency is high enough, the minority carriers of the inversion layer cannot respond and the measured capacitance would be that of the depletion region inside the semiconductor. The capacitance would decrease until the inversion layer screens any other increment of the bias and the measured capacitance reaches a minimum. This is called the *high frequency* regime.

A different case is when the bias is swept fast enough to make impossible for the minority carriers to form the inversion layer. In this case the depletion region expands until the breakdown is reached. This regime, called *deep depletion* is the one under which most of SCM measurements are made, because both the test signal and the sweeping signal are at high frequencies. All these considerations with the opposite sign of the C-V curves, are valid for p-type materials.

SCM Principles

The fundamental principle, for SCM measurement, is that the capacitance variation from accumulation to depletion, and its slope *dC/dV*, are inversely proportional to the free carrier concentration and their phases (signs) depends on the doping type of the investigated material.

In order to achieve a high spatial resolution, a high capacitance sensitivity is required. For a normal SCM tip with a radius of 25 nm, suspended at 5 nm from the sample surface, the tip/sample capacitance is approximately an attofarad (10^{-18} F).

It is extremely difficult to measure such a small capacitance, but measuring its dynamic change, *dC/dV* where V is the applied voltage, is possible . A first demonstration of SCM was given by Matey and Blanc[20] with a resolution of 0.1 by 2.5 μm. Further developments[21,22,23] have brought the normal lateral resolution to 20-30 nm and in under 10 nm with special tips[24].

The essential part of SCM is an UHF oscillator, with a frequency of 915 Mhz, coupled to the detector through a resonant circuit. The tip is grounded to the casing of the resonator circuitry and the UHF potential is applied to the sample which must have an ohmic contact (see Figure 11).

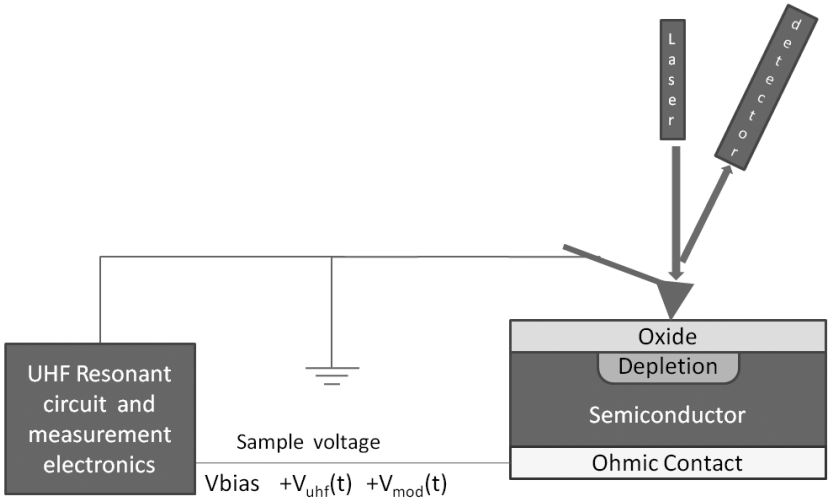

Figure 11 Scheme of an SCM apparatus.

The precise resonant frequency of the whole circuit, shown in Figure 11, is determined by the total stray capacitance, which can vary for different sample zones. The sensor is set on the point of maximal slope of the resonant amplitude curve by using an electrical tuning system (varactor). When the set point is correct,

small tip/sample capacitance variation gives a linear change in the dc output of the sensor, by shifting the resonant curve (see Figure 12)

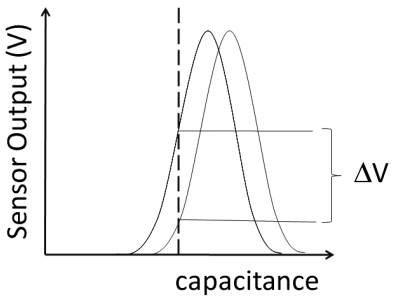

Figure 12 - resonant curve of the SCM measuring apparatus. Vertical line represent the set point for which small capacitance changes means measurable dc values.

Superimposed on the UHF signal (V_{UHF}) there is a second RF signal (V_{RF}) with controllable frequency and amplitude, respectively in the range of 5 to 100 Khz and 0 to 10 V_{pp}. This second signal is the one used to ramp the tip/sample bias in order to measure the dynamic change in capacitance *dC/dV* with $dV=V_{RF}$. In this way, a signal with the same frequency of V_{RF} and proportional to the capacitance variation can be collected by a lock-in. The latter supplies the dc signal whose phase and amplitude are used for image formation. Moreover, a fixed bias can be used to set the mean point on the C-V curve, on which the signal oscillates with amplitude V_{RF}.

For a fixed bias, the capacitance, or the depleted volume, can change for multiple causes, such as topographic variations, varying distance between tip and the sample local oxide thickness changes, or local variation in the semiconductor carrier density. However, generally, the probed volume has a lateral dimension comparable to the average tip radius. The vertical dimension of the probed volume is generally comparable to the lateral one. If the sample has a high carrier density, however, like in the case of a conductor or a highly doped semiconductor, the vertical dimension of probed volume may be much smaller than the tip radius.

The distance between the tip and the sample is maintained fixed through a contact force feedback given by photodiodes sensible to tip deflection by means a laser light reflected by the tip. This allows, through the recording of such feedback, to obtain morphological images (this is what is done in a normal contact-AFM measurement). The capability to acquire simultaneously the morphology and the SCM data is a powerful asset for two dimensional profiling, because accurate knowledge of tip location on a sample is critical and can often be identified by topographical features in the AFM image.

At the end of the measurements we will have three images like in Figure 13, one AFM image, one with the amplitude of *dC/dV* and one with the phase of *dC/dV*.

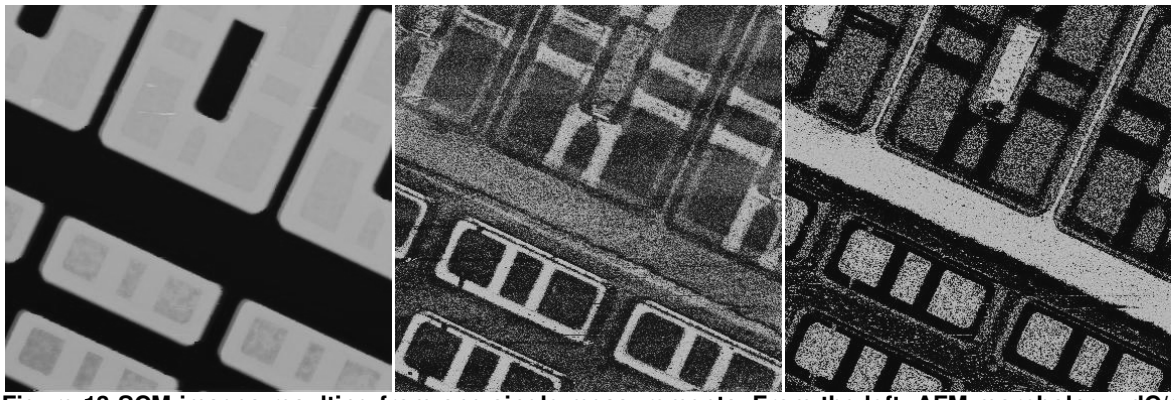

Figure 13 SCM images resulting from one single measurements. From the left: AFM morphology, dC/dV amplitude and dC/dV phase (black indicates n-type doping). Scan size is 20µm, DC bias is 0, AC amplitude and frequency are 1 V and 90Khz. The sample is a CMOS RAM memory device. Different doping densities and types are visible.

In the dC/dV amplitude image we can see the relative value of local free carrier concentration, which will be inversely proportional to the signal amplitude. In the dC/dV phase image we can associate the doping density previously found with the doping type.

It is important to know that the doping information can only be qualitative. Quantitative information can only be gathered after numerical simulations and signal calibration are performed[25,26].

What we have seen so far is an ideal scheme.

The C-V relationship changes as we consider, instead of1D MOS theory, the 2D or 3D MOS cases, with the metal electrode represented by a conductive AFM tip. Now fringing fields play a major role. In this case the variation ΔC from accumulation to depletion is smaller and also the slopes are different. This is the reason why numerical simulation are necessary.

Moreover, we have neglected some important effects that interface states and interface charges have on the C-V characteristics.

Interfacial states, between the semiconductor and oxide, that we have already encountered in the introduction to Schottky barrier, have no important effect on SCM measurements which are performed at high frequencies where such deep states cannot respond.

However, for what concerns the superficial charges these can be created by the oxide, by the dangling bonds of semiconductor surface, or by fixed or mobile

contaminants ions present on the sample. Their effect cannot be neglected and consists mainly in a shift of the C-V curve due to their fixed electrical charge. If the mobile ions are present, the effect is the drift of the C-V curve with time because they are attracted or rejected by the biased tip.

Another fundamental effect, present if surface charges contribute with a sufficiently high electrical field, is the creation of a permanent inversion layer under the oxide[27]. Such layer can produce a misjudgement of the doping type, which means that if the tip is on an n-type material what we can see is a phase signal pertaining a p-type semiconductor.

For what we have seen so far, a good oxide layer, with a constant thickness in the range of few nm (1-4 nm) and low charge density is required for reliable measurements.

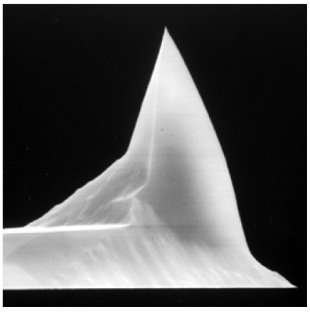

Figure 14 SCM tips used in this work. They are commercial SCM-PIC, with an n-doped Si cantilever with a Pt/Ir coating. The mean tip radius is 20 nm with 25 nm as a maximum.

In this work preliminary results have been carried out with a DI Dimension 3100 SPM equipped with the SCM add-on. The tips used , shown in Figure 14, are commercial SCM-PIC which consists of a cantilever of Antimony n-doped Silicon with a Pt/Ir coating. This coating serves as an electrical contact on the tip side, and as a reflector for the laser on the other side. The mean tip radius is 20 nm with a maximum of 25 nm. It worth noting that during the scans, due to contact between the tip and the sample, the radius increases.

SAMPLE PREPARATION

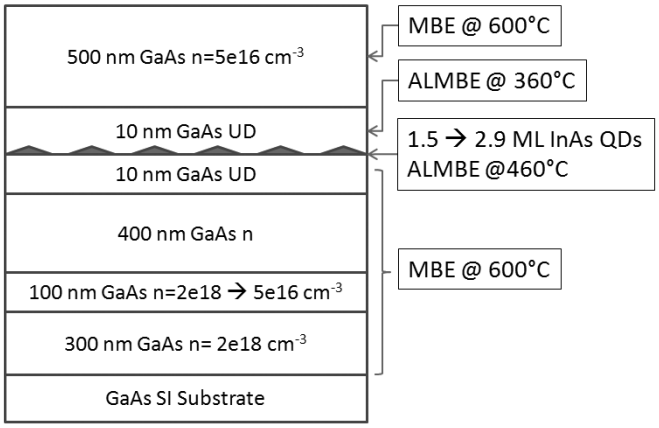

Figure 15 Samples structure

On (001) epiready 2 in. GaAs semi-insulating substrate, 300 nm of GaAs with a n-type doping density of $2x10^{18}$ cm^{-3} and 100nm of GaAs with a graded doping from $2x10^{18}$ cm^{-3} to $5x10^{16}$ cm^{-3}, are grown at 600°C. At this point 400 nm of GaAs with n=$5x10^{16}$ cm^{-3} is deposited at same temperature. Then, 10 nm of lower confining layer of undoped GaAs is grown at 600°C. Now a first growth interruption of 90 sec is done to reduce temperature at 460°C, and InAs quantum dots, with varying coverage along slice diameter, are grown.

After this, another growth interruption is used to diminish the temperature to 360°C in order to grow the upper confining layer of 10nm of undoped GaAs. Temperature is raised again to 600°C while completing the structure with a 500 nm thick cap of n-GaAs with a doping level of $5x10^{16}$ cm^{-3}.

The continuous variation of the amount of InAs coverage was obtained by interrupting the rotation of the sample holder during the InAs deposition. The coverage amount dependence on position was calculated taking into account the angle between the effusion cell and the substrate normal axes. The two substrates 2 inches wide used, allowed a coverage range of 1.4ML going from 1.5ML to 2.9ML. Estimated coverage values were verified by X-ray diffraction[28].

At the end of growing process, quantum dots formation is confirmed by photoluminescence measurements carried out at 10K.

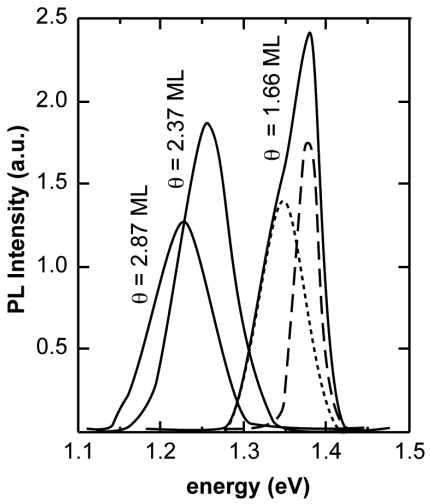

Figure 16 PL spectra taken at 10K, for samples with coverage values of 1.66, 2.37 and 2.87 ML. For 1.66 ML the peak has been deconvolved in Gaussian components. (Ref. Errore. Il segnalibro non è definito.**)**

In Figure 16, PL spectra are presented for different coverage values. The emission is attributed to optical transitions between ground states. The peak of 1.66 ML, near the critical coverage for 2D/3D growth mode transition, is deconvolved in order to show the coexistence of quantum dots and their precursors at the initial stage of 3D growth[29,30]. For higher coverage the emission energy shifts to lower values due to the enlargement of coherent islands.

After the MBE growth, samples have been prepared for electrical investigations. Such preparation consists in to the fabrication of Schottky diodes to be used as test devices for capacitive techniques.

After the cleavage of five 5x5mm pieces along the 2 inches wafer diameter, these samples are cleaned in a hot solution of Tricholoethylene , followed by Acetone and Isopropyl alcohol. After every bath, samples have been dried with N_2 flux.

At this point the samples are ready for ohmic contact preparation. Owing to the use of SI GaAs, planar Schottky barriers, with rectifying and ohmic contact both on the GaAs cap, were formed by photolithographic techniques. The procedure consists of a deposition by spinning of positive photoresist on the GaAs cap, annealing at 90°C for 30 min, and to UV light exposition under a quartz mask with an array of dots 500 μm in diameter.

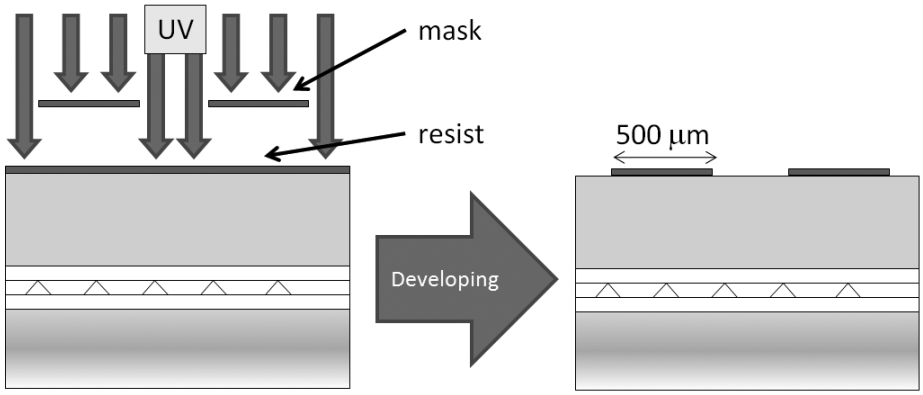

Figure 17 Developing process after UV light exposition in order to obtain dots of resist 500µm in diameter.

After the exposition, a developer is used to remove the exposed photoresist, as in Figure 17.

Successively, the ohmic contact is formed by evaporation, under UHV, of 70nm of AuGeNi on the regions where the resist was removed.

Then the samples are placed in a bath with Acetone to remove the unexposed photoresist, and the alloy deposited on it, a process called *lift-off,* as shown in Figure 18.

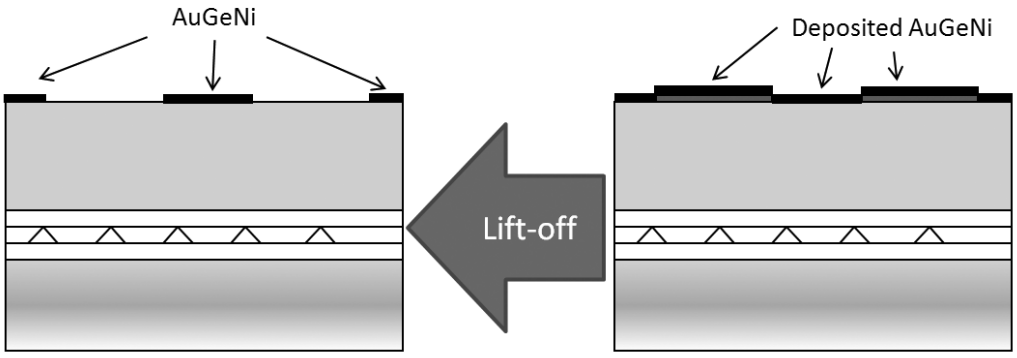

Figure 18 Unexposed photoresist removal, after AuGeNi deposition. Ohmic contacts are created, leaving free dots for Schottky barriers.

An annealing in N_2 flux at 350°C for 1 minute is then used to diffuse the alloy in the sample and to create the low resistance contact.

At this point, the Schottky barriers are fabricated with a second exposition with a mask having an array of transparent dots of 400 μm in diameter, which are centred in the previously made holes.

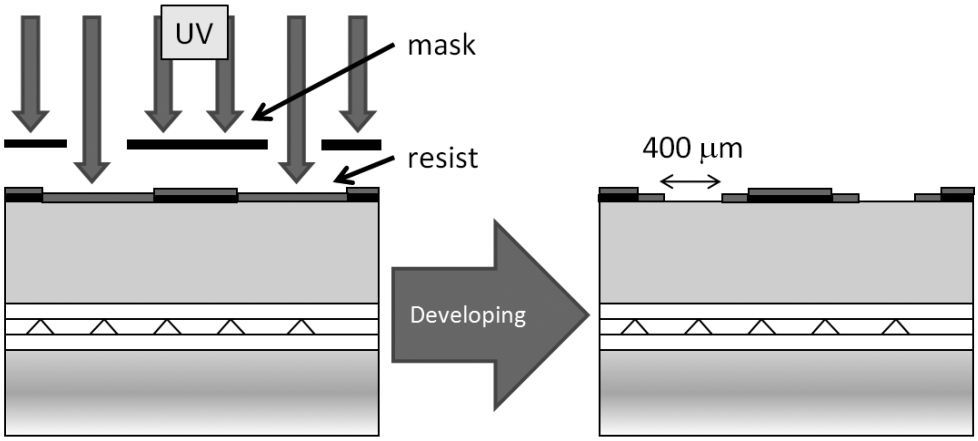

Figure 19 Photoresist UV exposition and developing for Schottky contact (Au) deposition

Before the Au deposition in the evaporator an HCl etching is used to selectively remove oxides from the GaAs surface. The concentration of solution is 37% in volume, and the duration is 15 sec, with stirring.

After the Au deposition acetone bath is used to remove the resist and then the excess of gold on the resist, leaving Au dots surrounded by ohmic contacts.

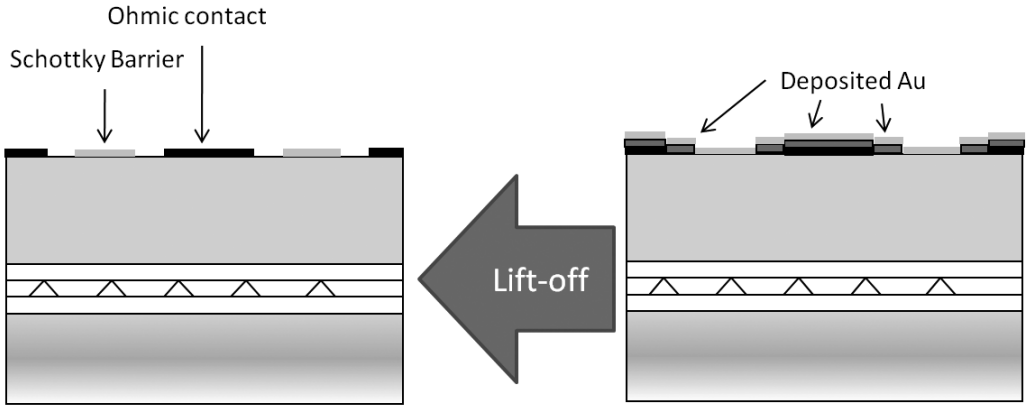

Figure 20 Lift-off process after Au deposition. After this step, samples are ready for testing.

It is important to know that in order to carry out capacitive measurements near the QD region (and to have the Au/GaAs interface nearer to QD plane), some samples have been partially etched prior the photolithographic procedure. The etching used was a solution with citric acid and hydrogen peroxide in the proportion 10:1. The bath used was at a temperature of 23℃ and the time used was 52 sec., resulting in a GaAs etching depth of about 0.2μm.

At this time samples are ready for testing. In this phase the I-V characteristics are tested with a Keithley 236 source measure unit.

Such curves taken at various coverages on our samples are shown in Figure 21. This graph demonstrates that diodes prepared on such samples are good enough for reliable electrical measurements, showing low leakage current in the bias ranges used. Breakdown voltage is higher enough in order to allow a good excursion of space charge region through the sample.

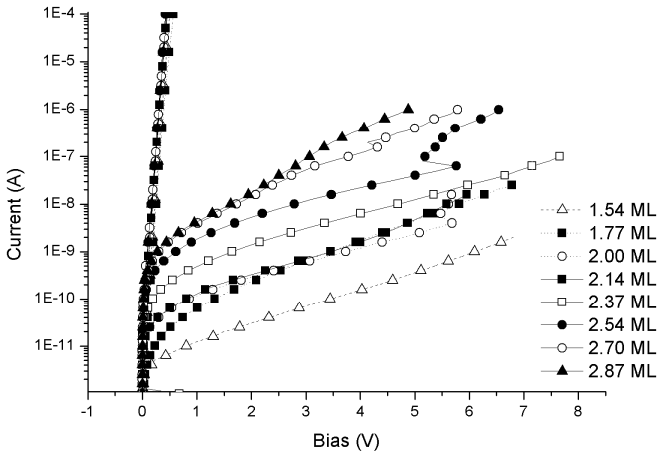

Figure 21 I-V characteristics obtained from samples in the coverage range between 1.54 and 2.87 ML. Measure performed ad RT.

In the end, samples are cleaved again to fit onto TO-39 metal package to which are fixed with silver glue.

An ultrasonic soldering machine is used to fix gold wires to TO-39 pins and a two-components conductive glue is used to fix the other wires ends to the diodes.

Now sample is ready for capacitive measurements.

C-V measurements where performed by a 4192HP impedence analyzer while DLTS measurements were taken by a high sensitivity lock-in type spectrometer.

RESULTS AND DISCUSSION

To understand the detrimental role of electrically active defects in electronic devices and, particularly, in quantum dots structures, we can look at the Figure 22.

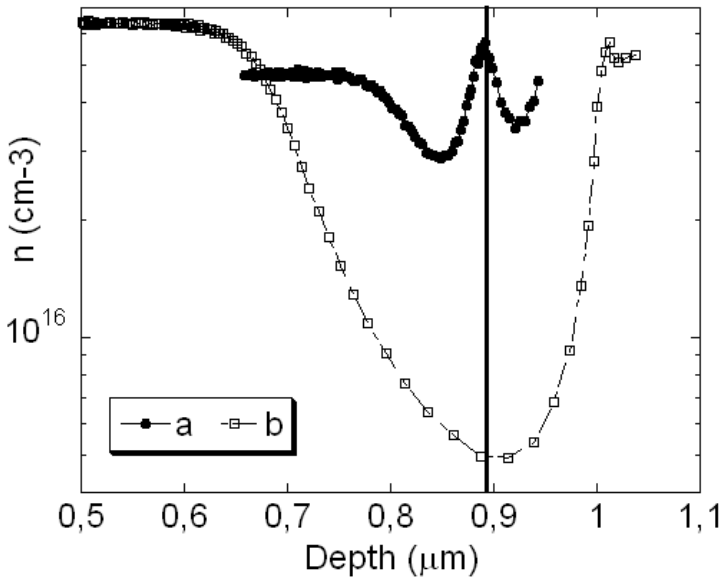

Figure 22 CV profiles of a) sample with accumulation peak b) depleted sample. The black line shows the QDs plane position.

This figure shows C-V profiles of two samples with same nominal structure. Depths are different from the one depicted in sample section because structures reported here were no more used for further experiments, but were really representative of the different electrical behaviour originated by the same nominal growths.

Starting from curve a), we can see a carrier profile characterized by three zones[31]. From the left, we have a first constant concentration corresponding to the cap distant from the QDs plane. Going deeper in the profile a peak surrounded by a depletion is found. This depletion goes down to $3x10^{16}$ cm^{-3} in the part facing the surface and $4x10^{16}$ cm^{-3} behind the peak. After this second zone we find the third and the last, the one referring to the buffer zone with a constant doping. This third zone is little or nothing represented in the CV profile because of breakdown limit of the Schottky barrier and also for the screening effect of the accumulation peak[31].

These effects pose a limitation to the extension of the depletion region of the Schottky barrier after the edge of the depletion region has crossed the peak position.

The origin of this peak is a carrier accumulation in the sample. More precisely this accumulation take place in the plane of quantum dots. Generally speaking a carrier accumulation can have two different origin (neglecting, deep states). The first is a δ-doping region, in which a thin plane in the sample has a high doping, resulting in a localized high carrier concentration. The second pertain to the quantum confinement effects. In this case, different materials with their different band-gaps are used to confine carriers in a small region. Normally this region is a 2D plane, both in the case of 2D quantum wells, or quantum dots laying in a plane. We can distinguish between these two causes by looking at the behaviour of the peak. One of the first index of quantum confinement is the full width at half maximum (FWHM) of the peak. Indeed, it is observed that FWHM of accumulation peaks we find in structures containing quantum wells or a plane of quantum dots, shows a strong temperature dependence. This, in turn, reflects the strong temperature dependence of Debye smearing out between the 2D and bulk carriers. This Debye smearing of the C-V profile does not necessarily occur in δ-doped structures because the carrier localization is achieved by the band bending associated with a high localized donors concentration[32]. Figure 24 shows the temperature dependence of FWHM and Peak height taken from accumulation peak of Figure 23.

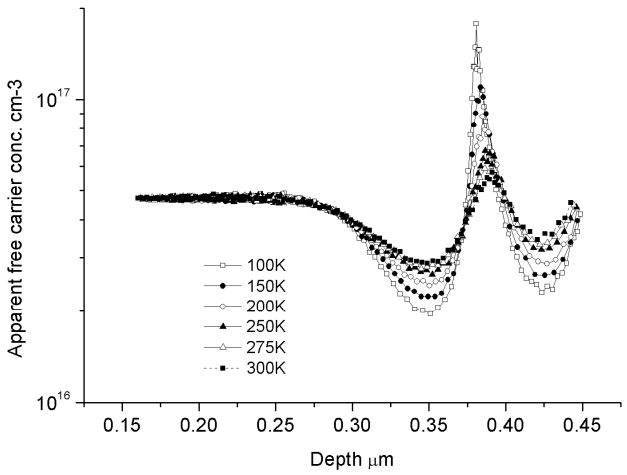

Figure 23 CV profile of a sample showing an accumulation peak, taken at different temperatures.

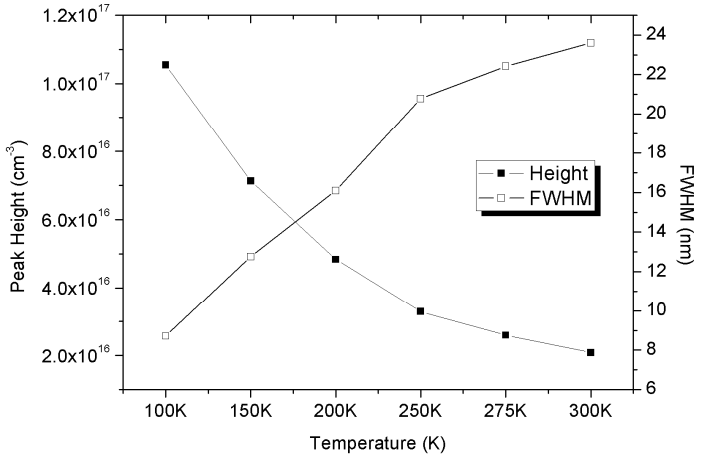

Figure 24 FWHM and Peak height Vs Temperature for accumulation peaks associated to quantum dots plane.

Moreover this level doesn't change his position while varying oscillation frequency of the capacitance meter in all the investigated temperature range, which means that the level is really fast and shallow just has those found experimentally and theoretically in literature for QDs levels.[33,34]

Last, as we can see In the Figure 23, the peak increases as the temperature decreases, in agreement with the hypothesis that Fermi level is raising and filling more quantum dots at different energies because of the Gaussian distribution of 3D island size.

Going back to the Figure 22 curve b), here we can recognize three zones too. The one corresponding to the cap, the one corresponding to the buffer, and the third in between. Nonetheless the difference is clear, the last zone mentioned shows a deeper depletion than that in curve a) going down to $5x10^{15}$ cm^{-3} instead of $2x10^{16}$ cm^{-3}, and it is also wider extending for 0,3µm instead of 0,05µm. Those are big differences but the most important one is the absence of an accumulation peak at the QDs plane depth. As said before, this absence is the main cause of this thesis, and the reason is that those samples were growth with the same nominal parameters. Same parameters, such big difference in electric characteristics.

Starting from this fact, we can begin our attempt to explaining the possible mechanism behind this behaviour.

Why we have no accumulation peak in curve b)? If we now turn to the Figure 23 and its analysis previously made, we said that the Fermi level raising (or falling) is responsible for the height of the peak. Extrapolating this concept to the falling of

Fermi level, we can imagine that QDs would be emptied and the peak would disappear. This is exactly what could be happening in the case of a depleted sample. A reason for the Fermi level lowering is what is missing now. The hypothesis followed by this work is that the lowering of Fermi level is caused by carrier compensation due to deep electron levels. The following pages will be devoted to the demonstration that this hypothesis is not unrealistic and to show what is the possible origin of those deep electron levels.
We can start from the study of TEM images referring to samples that presented such a big depletion to search for defects that could introduce deep levels.

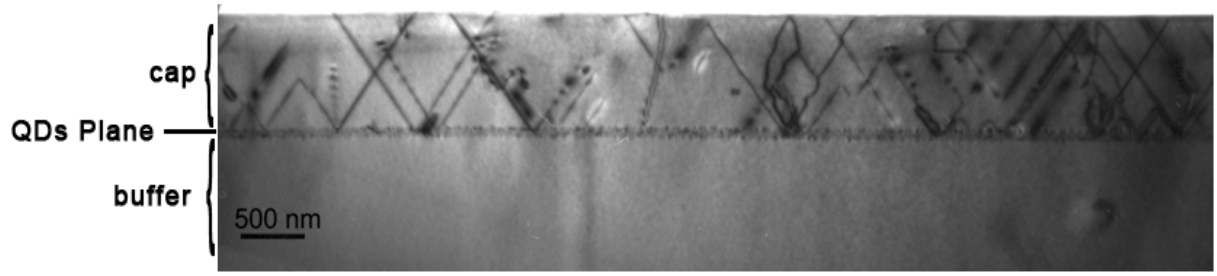

Figure 25 Typical cross sectional TEM image of depleted samples.

Figure 25 shows a typical cross sectional TEM image of a sample in which a depletion of free carrier is present. In this image cap and buffer regions are showed, separated by the tiny horizontal line in which Quantum Dots are situated. The picture clearly shows extended defects such as stacking faults and threading dislocations starting from the QDs plane and reaching the surface. Those defects are very easily responsible for the introduction of unwanted deep levels which not only compensate the material but also introduce non-radiative recombination centres which are detrimental for laser applications of quantum dot structures. So our goal is to reduce as much as possible their presence.
During the experimental work, in order to reach such a goal, we made the following hypothesis. Extended defects are caused by plastic strain relaxation so avoiding a strain excess should limit such relaxation. In the structure the principal strain source is the InAs plane in which the mismatch between this plane and the underlying GaAs make the formation of QDs possible, but also makes this plane really prone to stress accumulation and plastic relaxation. Further steps were made by keeping in mind that a key parameter of these structure is the emission wavelength of Quantum

dots which is strictly dependent from their size: the bigger the size (the 3D quantum well) the longer the wavelength (less quantum level separation in the well). Notwithstanding this, the size of quantum dots is likely to be the first responsible for strain relaxation so the higher the coverage amount the greater the criticality (this is a quite rough assumption in a complex subject, see for example ref.35). With this idea, a study of samples with gradually varying coverage from 1.5 ML to 2.9ML, has been carried out. By investigation of samples with this coverage range we could explore the evolution of quantum dots from their precursors at 1.5-1.6ML to islands bigger than those in the depleted samples mentioned above.

C-V Analysis

To appreciate the coverage importance become simple by starting the samples analysis with their C-V profiles reported in Figure 26.

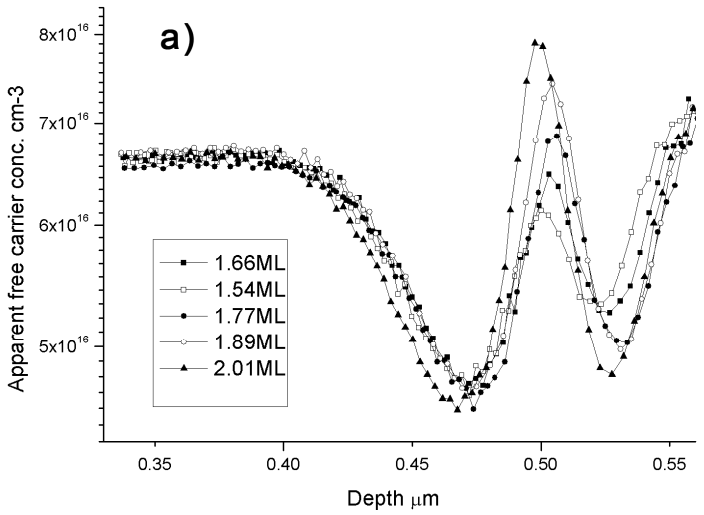

Figure 26 Room Temperature apparent free carrier concentration curves of QD samples with InAs coverage ranging from 1.54-2.01ML. The obtained profiles are shifted toward larger depth by 0.2μm, that is the amount of GaAs cap removed before Schottky contact deposition (Ref.36).

Figure 26 represent the C-V profiles of samples with coverage ranging from 1.54 to 2.01ML, taken at RT and with a test signal frequency of 1MHz. Accumulation peaks centred at the depth of QDs are clearly visible. Visible is also the increase of the peak height with the coverage. Starting from 1.54ML a peak is visible reaching a carrier density of $6x10^{16}$ cm^{-3}, while at 2.01ML accumulation reaches $8x10^{16}$ cm^{-3}.

Since we have attributed this accumulation peak to electrons confined in QDs and/or in the wetting layer, the above behaviour is likely due to the increase of QDs density and size, as confirmed by AFM measurements (Figure 37 p. 66). The increase of QD density gives rise to an increase of the emitted carriers from the dots located under the Schottky contact, while the increase of QD size is expected to lower the QD ground state energy level with respect to the GaAs conduction band, thus favouring the occupancy of the level by electrons.

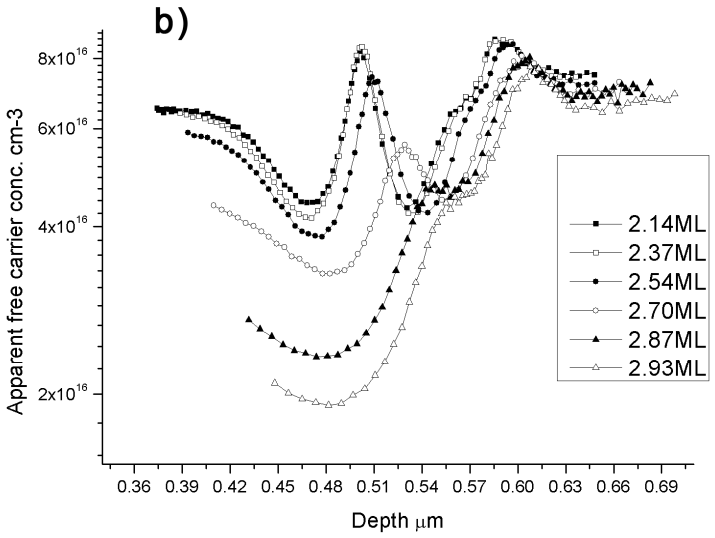

Figure 27 Room Temperature apparent free carrier concentration curves of QD samples with InAs coverage ranging from 2.14-2.93ML. The obtained profiles are shifted toward larger depth by 0.2μm, that is the amount of GaAs cap removed before Schottky contact deposition (Ref. 36).

For what concerns graph (b) of Figure 26, in this graph C-V profiles are taken from samples with coverage ranging from 2.14 ML to 2.93 ML.

The first two profiles, referring to 2.14 and 2.37 ML, have the same peak height but the latter has a lightly deeper and wider depletion, meaning that something is changing. By increasing the coverage the accumulation peak decreases and the depletion became deeper, ranging from a minimum of $4x10^{16}$ to $2x10^{16}$ cm^{-3}, until, for 2.87 and 2.93 ML, all cap is depleted and peak is almost invisible. These two effects can be explained by the same fact: there is the strong evidence that the free carrier density of the sample starting from the InAs plane through the cap is diminished because carriers are captured by deep acceptor levels[37,38], and consequently quantum dot levels cannot capture and accumulate carriers due to the Fermi level lowering. The density of those trapping centres is strictly correlated with

InAs coverage, and by what we have seen so far, 2.37 ML is the critical value beyond which the free carrier depletion increases.

Current-Voltage analysis

Another confirmation of the presence of deep centres and their correlation with coverage comes from J-V characteristics shown in Figure 28.

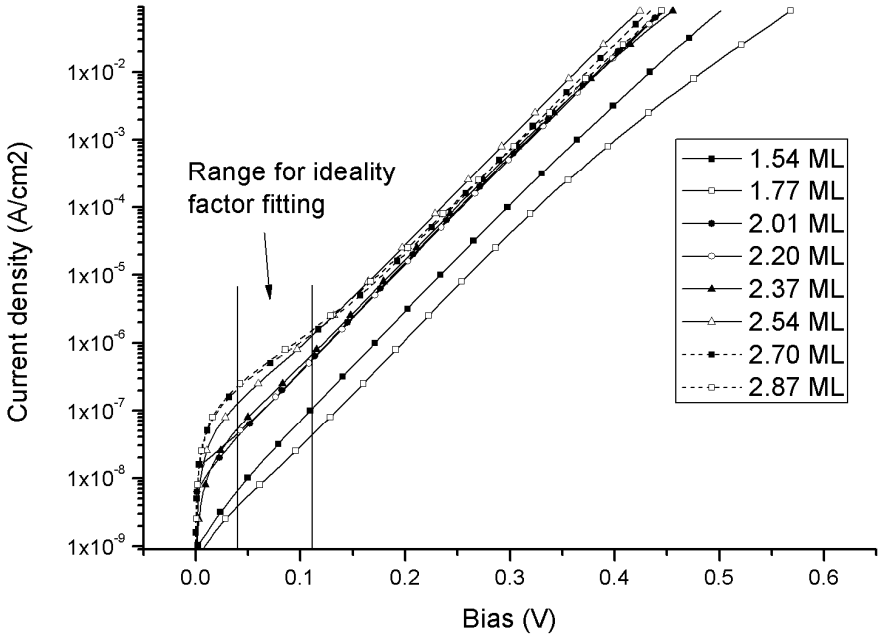

Figure 28 Current density Vs direct bias of samples with varying coverage. Also shown, the range fitted to obtain the ideality factor. (not all data points are shown for clarity)

We used the direct bias J-V curves fitting to obtain ideality factors versus coverage. In the initial part of bias range, current is due to recombination centres (in direct bias) and diffusion effects. We can have an indication of their relative weight by looking at ideality factor which is n=2 when only generation-recombination processes comes into play and n=1 when we have only carriers diffusion.

With this in mind we can look at Figure 29.

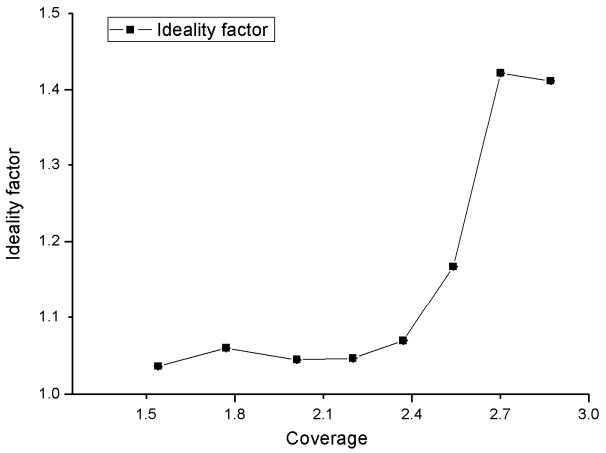

Figure 29 Ideality factor n Vs. Coverage. Is clear the fast increment starting at a coverage around 2.4 ML

This graph reports ideality factors obtained by fitting curves in the range shown in Figure 28. As we can see *n* remains quite constant and near 1 for samples with coverage from 1.54 ML to 2.37 ML. Then, starting from the latter coverage a very fast reaching of n=1.4 is evident. The correlation of higher ideality factor with deep centres (through the coverage) is clear and can be explained by recombination at those deep centres, or by recombination at interface states created by the same defects that could have originated the deep centres, whatever such creation has been due to etching process or not.

Deep Level Spectroscopy

In order to confirm the presence of those levels eventually correlated with coverage, a DLTS analysis has been performed on those samples. Our aim was to obtain information about the main electrical parameters of the deep levels present in the region between the Au/GaAs interface and the QD plane, and their concentration profiles. We have achieved this goal by using a particular DLTS method called Double DLTS. In DDLTS what is recorded is the difference between two normal DLTS signals referring to two slightly different ranges in the depletion layer. In this way is possible to study a “slice” of the space charge region and to obtain a profile of a level by moving this “slice” throughout the depletion region. There are different ways of performing DDLTS. The one used here maintains the reverse voltage V_r fixed together with the difference ΔV of the two filling pulses V_1 and V_2, while scanning the depletion region by varying their absolute value.

Results are presented for samples with coverage below and above 2.37 ML.

Figure 30 shows DDLTS spectra of a sample with 1.78 ML of coverage. The first spectrum (with V_r=-3.7V) refers to the cap of the sample far by InAs/GaAs interface. The others spectra are taken with biases such that the region near the QD plane was investigated.

As can be seen from the first spectrum, in this sample, the cap has no detectable deep level.

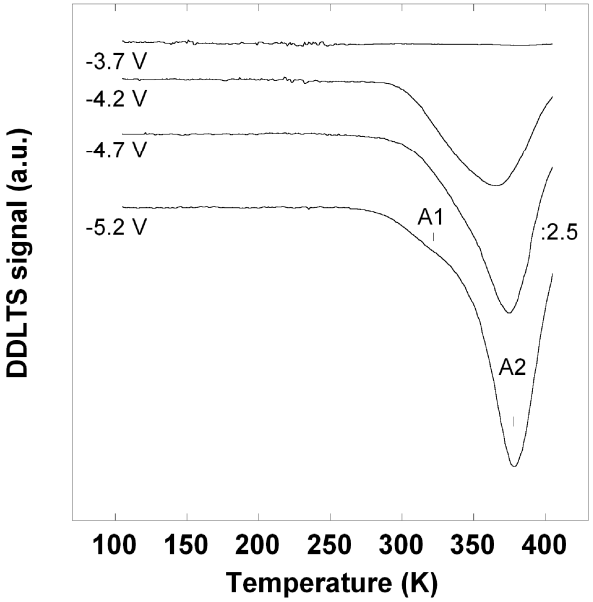

Figure 30 DDLTS spectra of 1.78 ML etched sample. The spectra are vertically shifted for clarity. The quiescent reverse bias is Vr=−6 V and the difference between the two bias pulses is V=V1−V2=0.5 V. The pulse high values of V_1 are indicated in the figure. No DDLTS signal above the sensitivity limit of the DLTS apparatus has been observed for higher values of V_1, corresponding to investigated regions closer to the cap layer surface. The rate window is 76 s^{-1} (Ref. Errore. Il segnalibro non è definito.**)**

Moving to the interface zone, deep level peaks appear in the DDLTS spectra. We have identified two traps labelled A1 and A2 with activation energies of 0.56 eV and 0.76 eV respectively. Capture cross sections are 2.7×10^{-15} cm^2 and 4.7×10^{-14} cm^2 respectively; such big values are typically associated to non-neutral trap centres with attractive potential, but we have no other experimental evidences to go further in the potential analysis. Similar traps were already reported in literature by Kaniewska et al.[39,40] and attributed to point defect-oxygen complexes and EL2 family, respectively. Oxygen inclusion was demonstrated by Kaniewska with SIMS measurements that evidenced the presence of high density of Oxygen at the interfaces between two layers grown by MBE and separated by a growth

interruption. With EL2 family we mean a family of deep levels due to the same As anti-site point defect but surrounded by different ambient condition (strain)[41].

As can be seen from the C-V profiles referring to samples with under-critical coverage, Figure 26 (a), these levels are present in such a low concentration that cause no visible depletion.

In Figure 31 (a), we can clearly see a DLTS peak of a trap we called A3 which dominates the spectra related to regions in the cap, far from QDs. A small shift of the emission rate while changing electric field is present. This indicate a charged centre with an extended interaction field[42]. Moreover the peak intensity and then he level concentration gradually increases up to 200nm from the surface and then slowly decreases going toward the QDs plane.

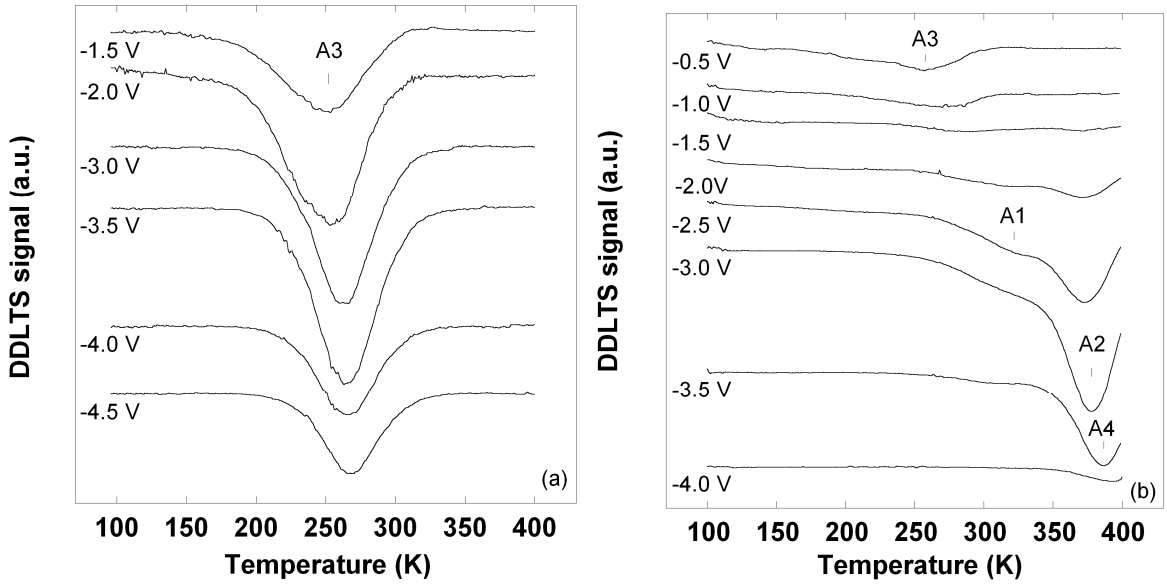

Figure 31 DDLTS DDLTS spectra of cap and QDs zones of a sample with 2.54 ML. The quiescent reverse bias is V_r=-5.5 and the difference between the two bias pulses $\Delta V=V_1-V_2$=0.5 V. The V_1 pulse height values are indicated in the figure. The rate windows is 76^{-1}. The spectra are shifted for clarity.(Ref. Errore. Il segnalibro non è definito.**))**

Its activation energy is 0.52 eV (measured at a mean electric field of $1.5x10^5$ V/cm) and the capture cross section is $2.5x10^{-14}$ cm^2. One of the most important feature of this trap is its logarithmic dependence of amplitude with the filling pulse width (Figure 33 (a)) which tells us that A3 is related to extended defects or clusters of point defects.

Figure 31 refers to only one value of coverage, but is interesting to look at the A3 DLTS signal for other coverages, which is shown in Figure 32

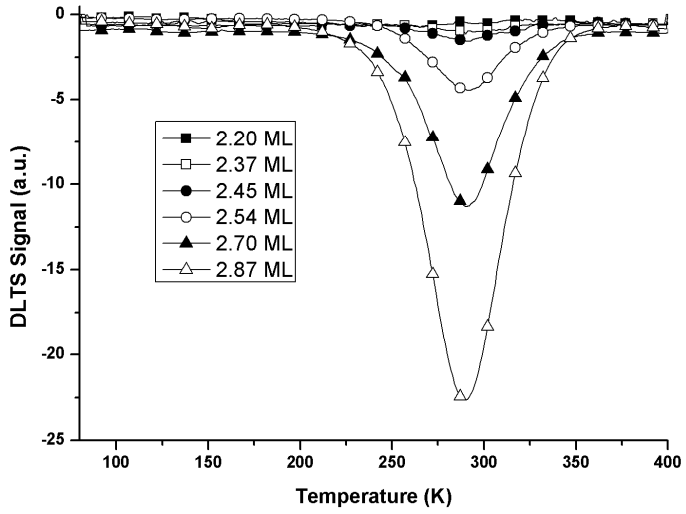

Figure 32 DLTS spectra of cap zones taken from samples with different coverage. Inset: DLTS peak amplitude Vs. Coverage

In this figure simple DLTS spectra are reported, which means that the measures were taken including a large region of the, without including the QD/GaAs interface layer. This is confirmed by the absence of other peaks in the spectra. We can clearly see that A3 peak signal raises with coverage.

Going towards the QDs plane (Figure 31 (b)) we see that the peak A3 disappears while three traps, labelled A1, A2 and A4 appear at higher temperatures. A1 and A2 are already known because they were present in the sample with a coverage of 1.78 ML. As for the third QDs plane trap, named A4, this is a new deep level we haven't seen before. Its activation energy is 0.84 eV and the capture cross section is about 2.7×10^{-13} cm^2. In this case too, we have seen a logarithmic amplitude dependence with the filling pulse width suggesting that it is related to extended defects.

Figure 33 (a) shows the dependence of the DLTS signal from the filling pulse width of traps A3 and A4, while in (b) A1 to A4 traps signatures are presented.

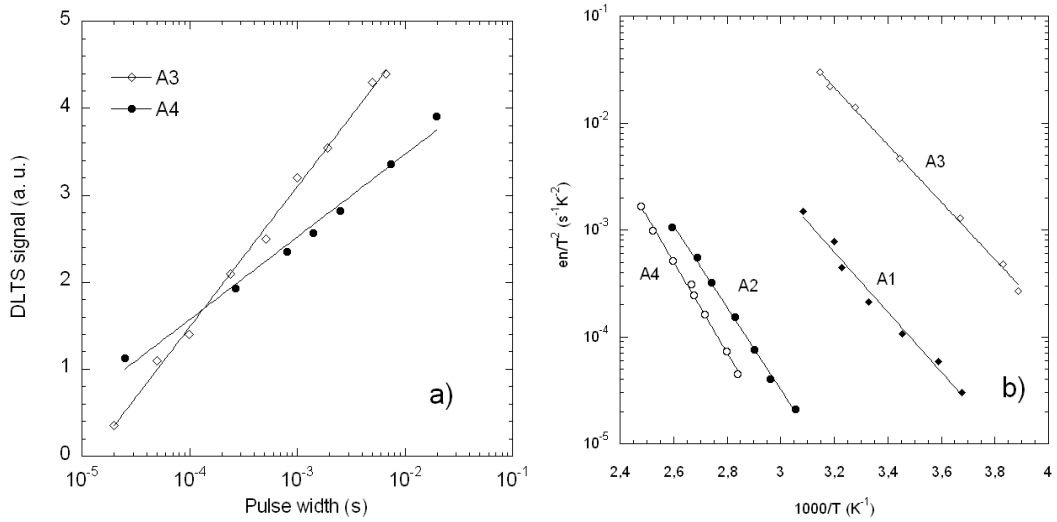

Figure 33 (a) DLTS signal amplitude Vs. Logarithm of Filling puls width for A3 and A4 traps (b) A1-A4 traps signatures. (Ref. Errore. Il segnalibro non è definito.**)**

Trap	Activation Energy (eV)	Capture cross-section (cm^2)
A1	0.56	$2.7x10^{-15}$
A2	0.76	$4.5x10^{-14}$
A3	0.52	$2.5x10^{-14}$
A4	0.84	$2.7x10^{-13}$

Table 1 Activation energies and capture cross sections of traps observed by DLTS

Other Analyses

In order to investigate the extended defect distribution in the above samples, TEM analysis has been carried out.

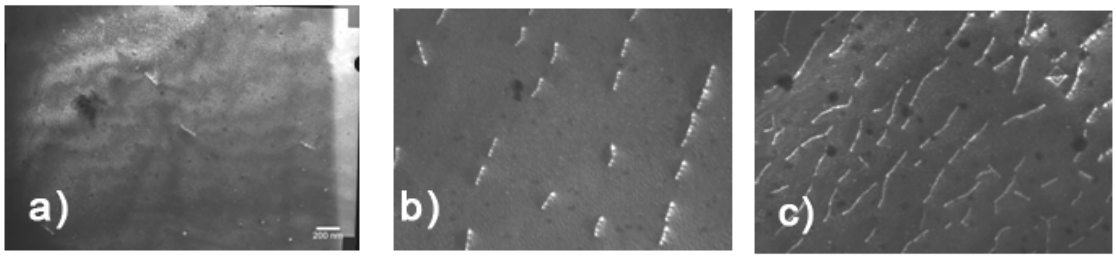

Figure 34 Planar TEM images of samples with different coverage (a) 2.37 ML (b) 2.57 ML (c) 2.87 ML (Ref. Errore. Il segnalibro non è definito.**)**

Figure 34 shows planar TEM images taken from samples with (a) 2.37, (b) 2.54 and (c) 2.87 ML of coverage. It is evident the presence of extended defects with raising density going from $6.1x10^7$ to $1.2x10^9$ cm^{-2} with increasing coverage.

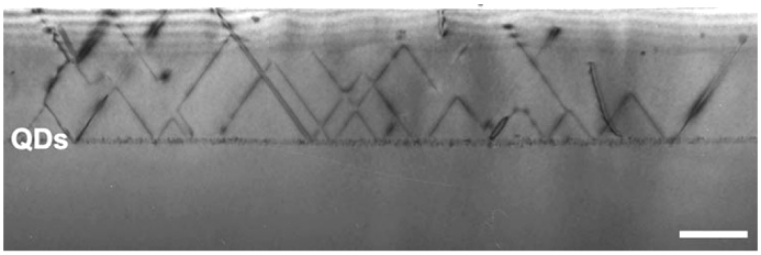

Figure 35 Cross sectional TEM of a sample with 2.87 ML of coverage, showing V-shaped defects distribution. Scale bar is 500nm

Looking at the Figure 35 which refers to a coverage of 2.87 ML, we can see two regions separated by a tiny line. This line is the plane of QDs, the lower zone is the buffer, while the upper one is the cap. This image clearly shows that extended defects starts from the QDs plane. Such defects are V-shaped defects that can reach the surface or annihilate reciprocally.

We can strictly correlate the A3 trap found in these samples by DLTS with the extended defects observed by TEM, because we found them at the same depths, and with the same distribution. In fact, both A3 amplitude and extended defects reach a maximum between the surface and the QDs plane (at about 200nm from the QDs). Moreover, the trap signal dependence with the filling pulse width tells us that A3 pertains to extended defects.

Each branch of a V-shaped defects is an edge dislocation (which eventually dissociate into two partials). In a III-V semiconductor material, with zinc-blende structure, line defects on the glide plane (such as those we found in our samples) contain dangling bonds that in an n-doped semiconductor behave as acceptor levels[43]. This would be consistent with the electric field dependence of A3 emission rate, nevertheless with Schottky barriers we cannot distinguish an acceptor level from a donor one, so this aspect has to remain an hypothesis until further studies are available.

As for samples with under-critical coverage, no extended defects were found, indicating an upper limit for dislocation density of $1x10^6$ cm^{-2}.

Another confirmation of the critical coverage values as the starting point for deep centres generation, comes from integrated Photoluminescence intensity. This measure integrate on all frequencies the photons emitted from the sample after electron-hole pairs have been created by optical excitation.

Quantum Dots are radiative recombination centres, this is one of their main feature, the one used for laser application. The recombination via photon emission is in competition with recombination via phonon emission (non-radiative recombination) and the latter happens in deep centres which are near the mid-gap (capture rate similar to emission rate). So photoluminescence efficiency is reduced by the presence of such non-radiative recombination centres in sufficient concentration.

By looking at Figure 36 this is exactly what we see. This figure shows integrated PL intensity versus coverage. It is possible to divide the curve in three regions. The first, from coverage of 1.6 ML to approximately 2 ML, in which the intensity rises up. This is consistent with the growing dynamics of quantum dots, which indicate 1.6 ML as the transition between 2D and 3D growth so in this first range QDs are just forming and their density is increasing.

The second range starts from about 2 ML and ends at about 2.4 ML. Within this extremes we have no significant PL intensity changes..

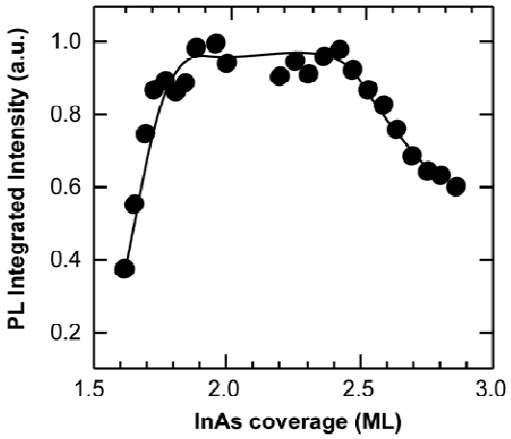

Figure 36 PL integrated intensity Vs. coverage. Measures taken at 10K. (Ref. Errore. Il segnalibro non è definito.**)**

The last range goes from 2.4 ML trough 2.9 ML. This is what we have regarded as the over-critical range, in which electrical and TEM characterizations have evidenced all defects we have talked about so far. As we can see, in integrated PL intensity too, there is a dramatic change. The lowering of PL intensity means that deep centres are acting as non–radiative recombination centres, stealing carriers for radiative recombination

Now a question spontaneously rises: what happen at the critical coverage of 2.4ML? A good answer is obtainable by AFM measurements on uncapped samples with the same nominal growing parameters.

By AFM images it is possible to count QDs and obtain the island density. Moreover, it is possible to measure the mean size of such islands and, by this, to have their size dispersion. Both this information were used to make the following graph

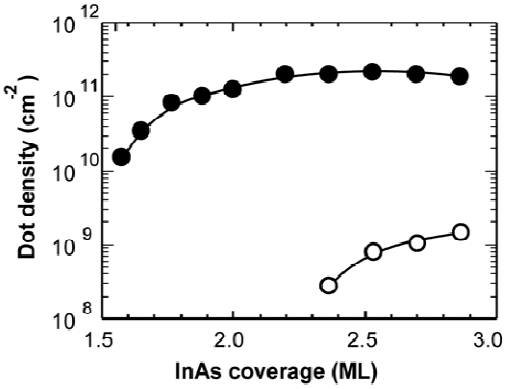

Figure 37 QDs density vs. Coverage, taken from AFM images of uncapped samples. Two curves are shown, the full circles refer to "normal" dots, while the empty circles refers to ripened quantum dots. (Ref. Errore. Il segnalibro non è definito.**)**

The graph reported in Figure 37 represents the dependence of QDs density with the coverage. The curves are two because QDs have been divided in two type: full circles refer to the normal one which forms first, with density from an initial value of about $1.6x10^{10}$ up to $1.10x10^{11}$ cm^{-2}. This density increases in the coverage range from 1.6ML to 2.0ML and above 2.0ML varies little. These dots have a diameter that starts from 6 nm for low coverage and stabilize on 15 nm. The height goes from 0.5 nm at low coverage to 2.7 nm for high coverage. The other curve, the one with empty circle, refers to larger islands that appears at a coverage of 2.37 ML with a density of $2x10^{8}$ cm^{-2} up to $1.5x10^{9}$ cm^{-2} for 2.87 ML. Their height starts at 4 nm and grows up to 6 nm.

The fact that those larger islands start to be present at 2.37 ML, the coverage we have identified as the critical one, is not a coincidence. What we think is that those islands are responsible for strain relaxation via misfit dislocations which, in turn, are the source of the V shaped defects we have seen in the TEM images.

The growth of those larger islands and their coexistence with the quantum dots, is theoretically explained in a study of Daruka and Barabàsi[44] in which a thermodynamic model is made starting from the Helmholtz free energy (at a fixed temperature). Energy of the wetting layer, 3D islands with a pyramidal shape, and

that of relaxed island, is taken into account. A phase diagram is obtained in dependence of the total coverage and the mismatch between the two materials of the heteroepitaxy. This phase diagram differs from the one we talked about in the MBE introduction section, because two transition coverage are identified. The first one is the transition between 2D and 3D growth mode when 3D islands starts growing quite abruptly (is a second order transition) and reach a fixed size that minimize their energy, this critical coverage was obtained also in the ref. 13. The second one, found by Daruka and Barabàsi, is at higher coverage with respect to the first, and represent the starting point of larger islands growing. Those island are incoherent (not adapted to the substrate lattice), and so relaxed. Their size has its minimum energy at infinity, so they grows bigger with increasing coverage. Their incoherence generate the misfit dislocations.

This incoherence is confirmed by other TEM analysis an image of which is showed in Figure 38

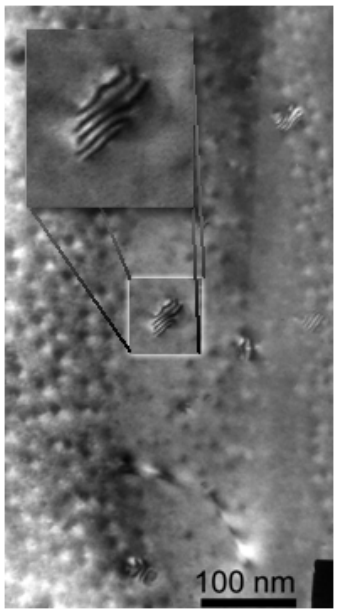

Figure 38 TEM images showing Moirè fringes created by a larger incoherent island.

In this image, Moirè fringes are clearly visible. Those are interference fringes due to electron diffraction by two different lattices with slightly different parameters. Their presence is a sign of incoherence between island lattice and the substrate one.

TEM analysis has shown that starting from their generation, the percentage of larger island that relax into the incoherent state soon became 100%.

What we think, is that these incoherent islands are responsible for defects generation, and that the critical coverage we found by so many analyses is the one pertaining the second phase transition that Daruka found.

A brief note on Stacking Fault Tetrahedra

In the earlier samples, at the start of our studies on those structures, a particular kind of crystal defect was singled out: the stacking fault tetrahedra.

Those defects have an interesting geometry from which they take their name.

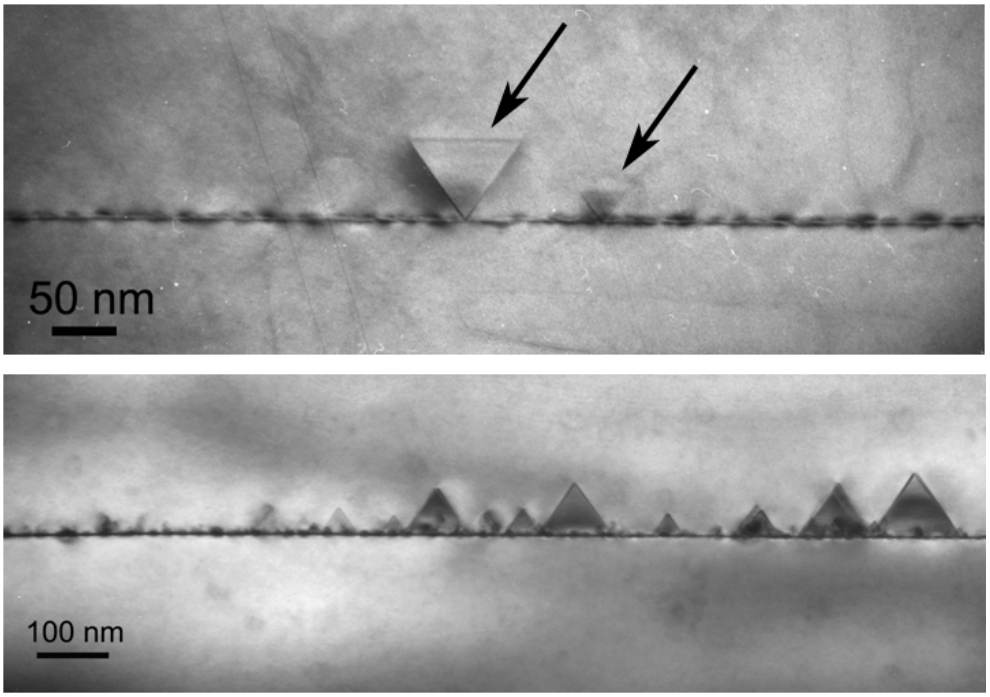

Figure 39 TEM images of Stacking Fault tetrahedra encountered in the first samples. The two images are taken from two different cross section direction.

Figure 39 shows cross sectional TEM images taken from two orthogonal planes, so that what we are seeing are two views of the same defect. Moreover, Figure 40 shows also a planar view. By trying to join those views in a single geometric object, the defect was singled out, and it was not a trivial task.

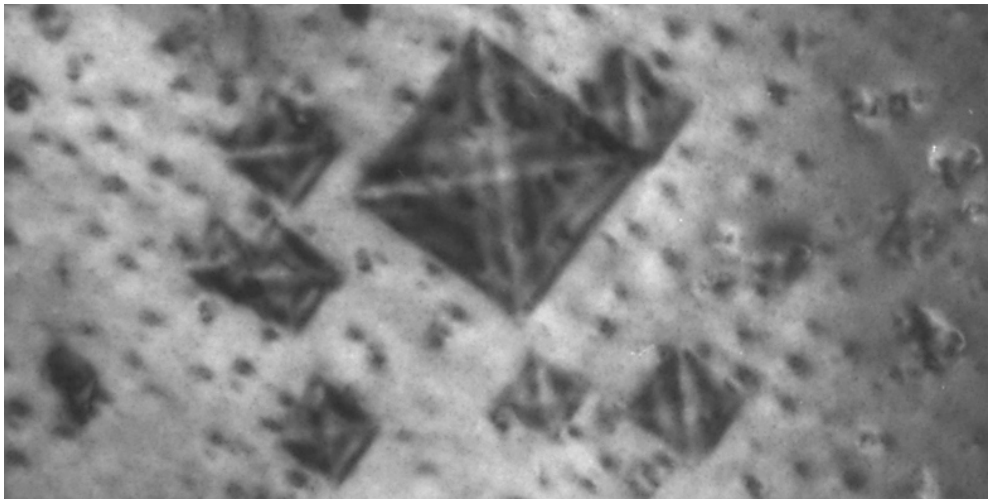

Figure 40 TEM Planar view of Stacking Fault Tetrahedra

To clearly understand the shape of such defects we can look at the Figure 41, where a simplified scheme of stacking fault tetrahedra (SFT) is presented and the view directions of Figure 39 are indicated. The edges of SFTs are partial dislocations surrounding the faces which consists of intrinsic stacking faults (an atomic plane is missing). Such stacking faults are on the glide planes, as usual, which in the zinc-blende are the {111} planes[45,46,47,48].

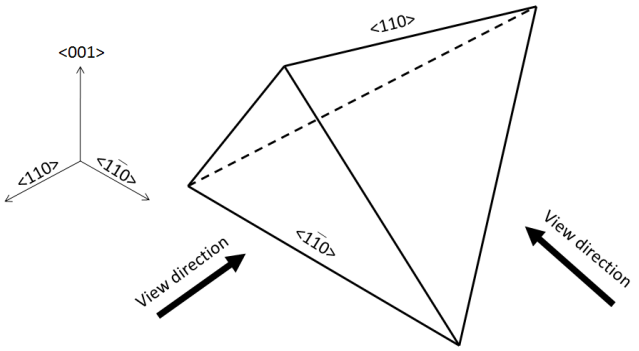

Figure 41 SFT scheme. Crystal directions are indicated, together with the cross-sectional TEM images view directions.

Their extension can be as great as 100 nm from the QDs plane, which is quite big because in their energy formation balance, SFTs are penalized by high stacking fault formation energy (especially in III-V materials). This latter energy gain as to be balanced by the edges formation. A mechanism has been proposed by Silcox and Hirsch, by witch those energy balance is favourable. In this mechanism the defect formation has to start from a platelet of vacancies (intrinsic stacking fault) [49]. In our samples, made of III-V materials, those vacancies should be on one of the {111} planes. It is difficult to know the exact formation mechanism applied to our samples,

nevertheless, it is interesting to note that, by the Silcox and Hirsch mechanism, the defects starts from an intrinsic crystal defect, so it seems that extrinsic contamination is not required and some kind of kinetic process is sufficient.
DLTS measurements were performed on those samples, and, referring to the region around QDs plane, the samples containing SFT showed a deep level with activation energy of 0.63eV and capture cross section of $5x10^{-15}$ cm^2. Actually, those values slightly vary from sample to sample but this is due to the fact that those starting samples had different doping levels, because they were used also to find the right device parameters. So we have no good statistics on SFTs and this doesn't allow us to be sure about their DLTS attribution. Yet, I found it interesting to cite them, because of the lack of literature on this topic, and because it is the first time they are reported in InAs/GaAs(001) structures (see for InAs/GaAs(111)A Ref. 50 and Ref. 51).

SCM preliminary results

In order to obtain local information and expanding the samples investigation possibilities, we have started the implementation of Scanning Capacitance Microscopy (SCM) in the study of our structures.
What we have obtained are preliminary results which demonstrates that the application of this technique on this kind of structure is possible.
One of the main SCM issue is the samples preparation, so a preliminary work has been done in finding the simplest conditions to obtain good trial samples.
Indeed, a smooth surface is necessary in order to obtain reliable results. The reason is that surface features can act as preferential oxide formation sites giving rise to a change in capacitance due to different oxide thickness, or, if they have dimensions comparable to the SCM tips, can influence the measured capacitance by means of geometrical factors. Both these effects can mask the doping information we want to obtain.
Moreover oxide can introduce spurious effects due to interface charges and states, that affect the measurements.
So, the key factors are two: smooth surfaces and an homogeneous layer of good oxide.

Many types of oxidation processes exist (plasma oxidation, wet oxidation, UV/Ozone oxidation, etc.) but, as a starting point, we decided to take into account only the thermal native oxidation process.

What we have found from literature is that for what concerns GaAs, there are important differences in the thermal oxide formation between the two main surfaces of our samples: the planar surface (001) and the cleaved surface (110).

For what concerns the surface (001), the thermal oxide grown at ambient temperature is formed by clusters of few nm height and tens of nm long. Moreover, the oxide morphology strongly depends on surface cleaning, etching etc[52].

As for the cleaved surface (110), the thermal oxide, after a virtually instantaneous formation of the first layer, slowly proceeds layer by layer. The thickness increases with the logarithm of storage time[52].

For what we have seen so far, we decided to start by cross-sectional analyses of our samples, by cleaving and exposing the (110) surface to the ambient atmosphere.

The sample structure analyzed is presented in Figure 42.

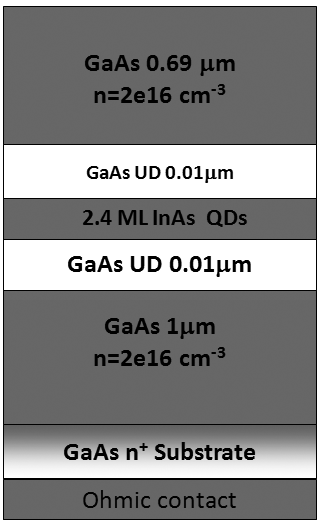

Figure 42 Structure of sample analyzed by SCM.

Successively, silver glue is used to fix the samples on a metal holder and to ensuring the electrical contact.

Our preliminary results are presented in Figure 43 and in Figure 44.

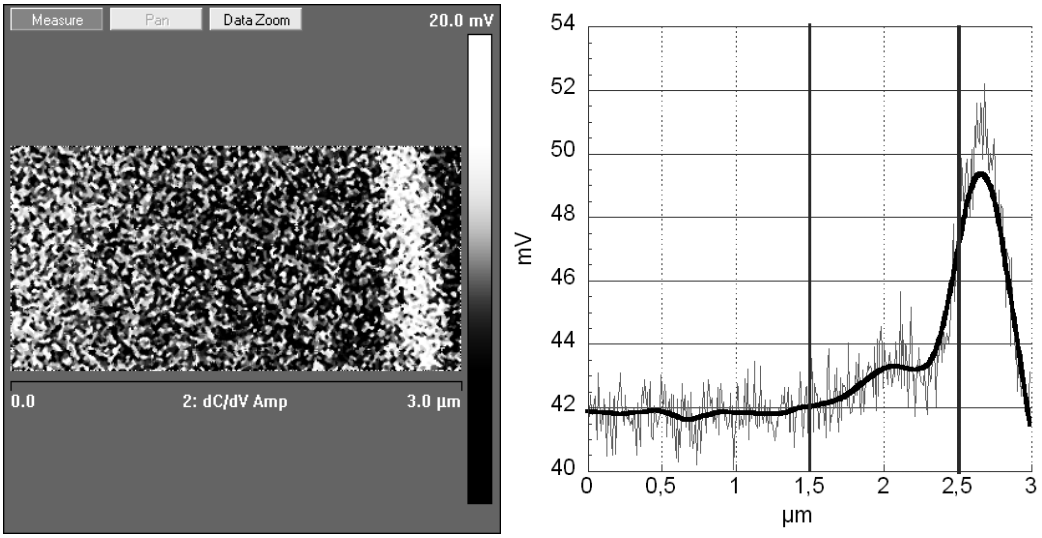

Figure 43 On the left, SCM image representing dC/dV signal amplitude. AC Signal amplitude and frequency are respectively 2V and 90Khz, DC Bias is 0V. On the right, the curve represent the mean values of dC/dV amplitude, obtained by mediating on image lines. Vertical lines indicates supposed substrate and QDs positions.

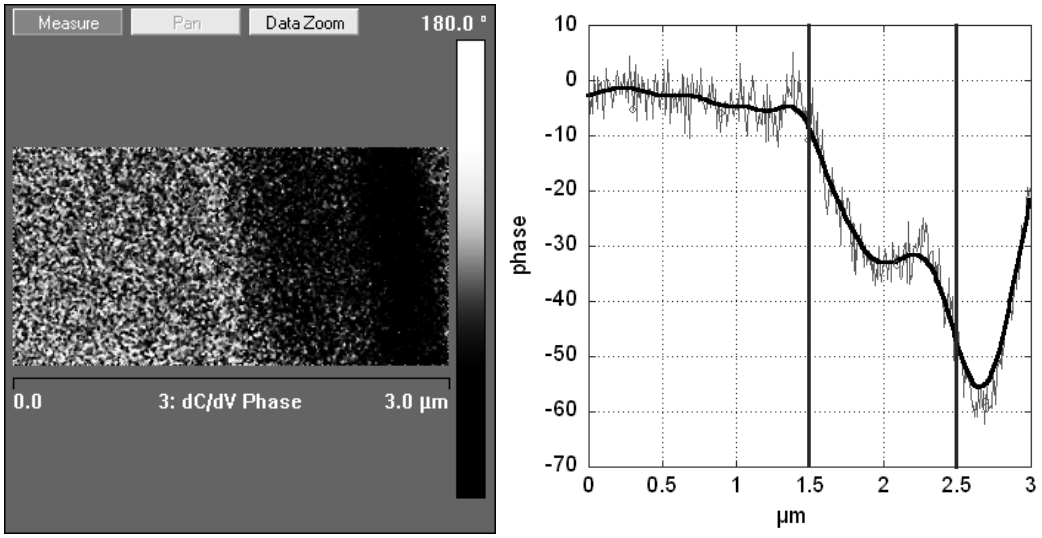

Figure 44 On the left, SCM image representing dC/dV signal phase. AC Signal amplitude and frequency are respectively 2V and 90Khz, DC Bias is 0V. On the right, the curve represent the mean values of dC/dV phase, obtained by mediating on image lines. Vertical lines indicates supposed substrate and QDs positions.

These images where acquired at four hours from sample cleavage. Figure 43 represents the dC/dV signal amplitude while the Figure 44 shows the phase of the same signal. Both images are recorded simultaneously. The graphs that are showed beside the images are obtained by a mean operated on all image lines. The orientation of the samples is such that the GaAs substrate is to the left and the sample surface is to the right, at an approximate distance of 180nm (because passing with the tip on the edge of sample can cause tip damages). Remembering that dC/dV signal amplitude is inversely proportional to the free carrier density, the

amplitude peak, that is visible in the graph of Figure 43 centred at about 2.65 μm, represents a depletion region inside the sample. We can find the same peak in the phase graph of Figure 44, but with the opposite sign. The negative phase of signal means the presence of a n-type doped material, consistent with the sample structure. A smaller depleted zone is visible in the graphs, between the two vertical lines where we supposed the presence of buffer layer. This would be consistent with a doping density of the buffer layer lower than the n^+ substrate and higher than that of depleted cap. The slow gradient of apparent free carrier concentration between substrate and buffer is not clear, and further studies are necessary to clarify this aspect.

In order to verify that the depletion region visible in the sample cap by SCM is the same we usually see with C-V measurements, we can make a comparison between the two profiles.

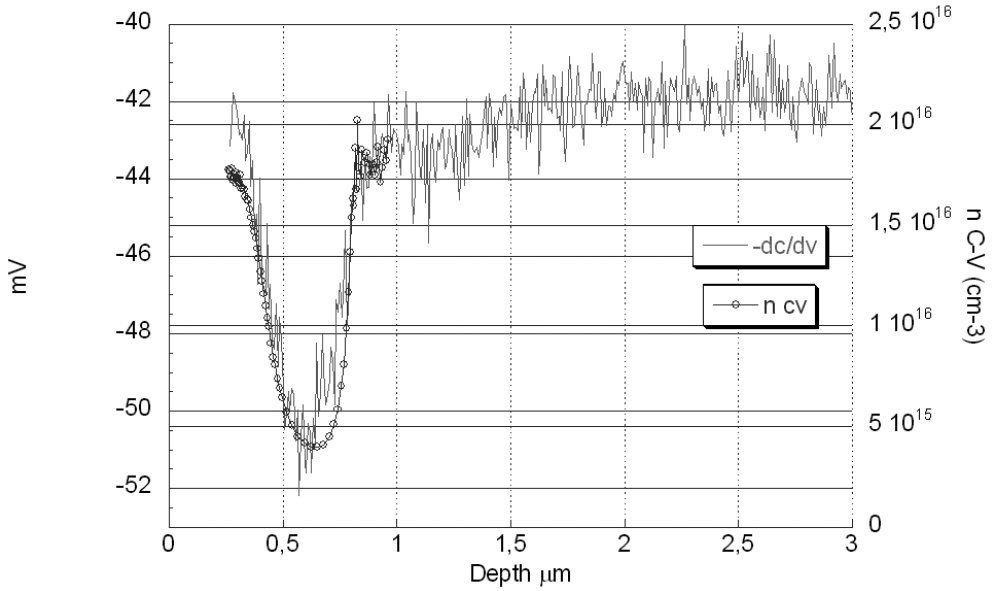

Figure 45 SCM and C-V profiles of the same sample. Reciprocal amplitude and position were adjusted in order to superimpose the two curves.

In Figure 45 amplitude axes have been rescaled and depths have been shifted, in order to superimpose the two curves obtained on the same sample. As we can see, the widths of the depletion regions present in both the profiles are similar and comparable.

Figure 45 suggests another important aspect of SCM. It is clearly visible the spatial limit of C-V profiling methods, subjected to the breakdown limit of the Schottky barrier, in contrast with the extension of the SCM profiles. The latter is limited only

by the image extension that is possible to achieve with the microscope (in this case 100x100 µm).

A drawback of SCM technique is readily available and presented in Figure 46.

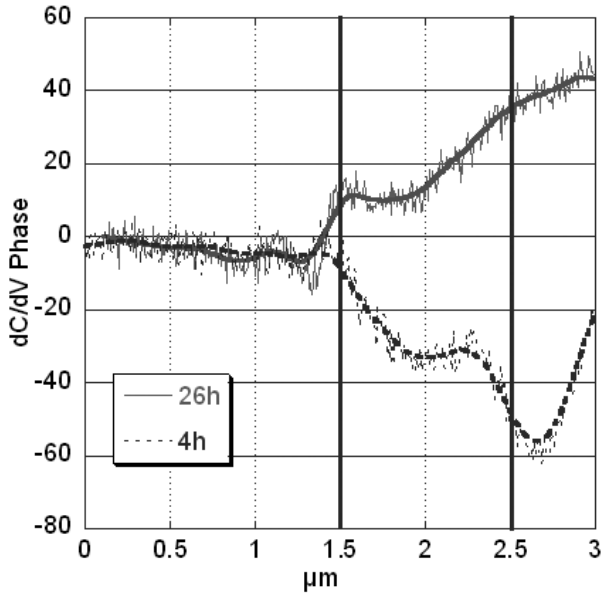

Figure 46 SCM dC/dV phase signal of the same sample measured at 4 and 26 hours from cleavage. Measuring parameters are the same.

In this image two dC/dV phase curves are reported. One has been recorded after 4 hours from cleavage and is the same of Figure 44, and the other has been acquired after 36 hours from cleavage. It is clear that while absolute values are similar, although the “4 hours” curve has somewhat more definition, the signal signs are opposite. As we know, the sign of dC/dV phase signal is directly correlated to the doping type of the region under the tip. With this Figure, we can clearly see the effect of sample ageing due to bad surface oxidation. This effect, known as “contrast reversal”, is due to oxide charges and their electric field that originate a permanent inversion layer in the semiconductor surface[27].

The bad oxidation of the sample after many hours is visible in the morphology image of Figure 47. On the left, the sample after 4 hours from cleavage, on the right the aged one, at 36 hours from cleavage. While in the former the surface appears smooth, in the latter, oxide clusters are evident with dimensions of few tens on nm wide and few nm hight. It worth noting that such clusters appear wider on the sample side grown by MBE, than that present on the substrate.

Further studies are on the run, in order to investigate different thermal oxide grown at different temperature, and to estimate the lateral resolution accessible by SCM technique on this kind of samples.

Moreover, a study by means of planar images on uncapped QDs or with other capping procedure that can enhance SCM contrast, is a must. Nevertheless this is subordinated by a good sample preparation procedure.

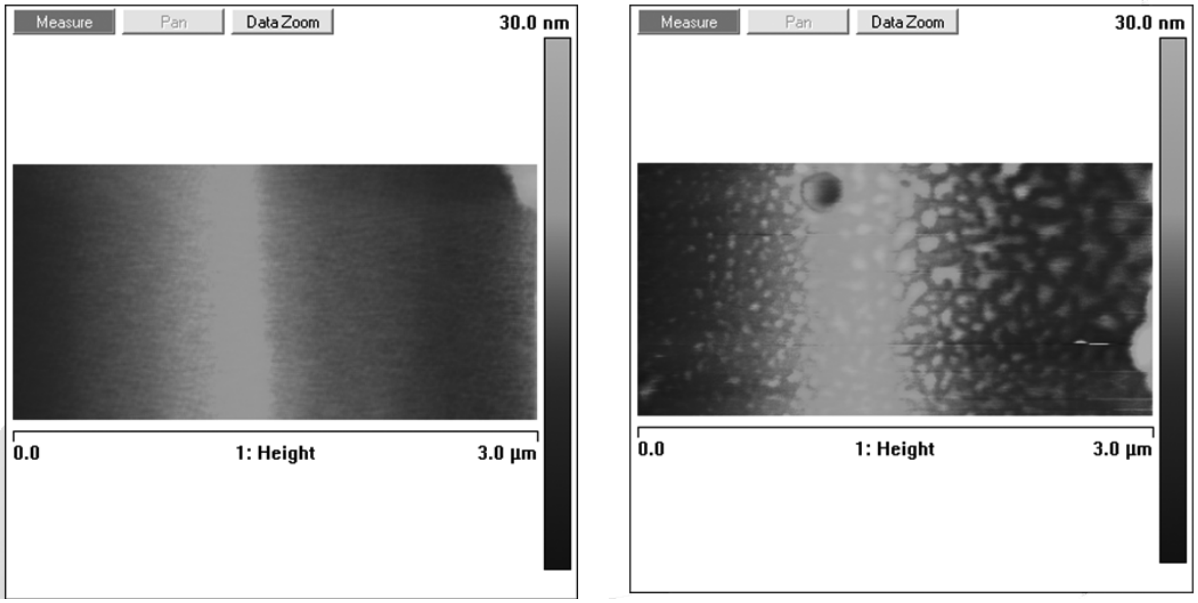

Figure 47 AFM image of samples surfaces after 4 and 36 hours from cleavage

CONCLUSIONS

At the end of this work of thesis, the origin of dislocations in InAs(QDs)/GaAs structure has been identified. Such strain relaxation mechanism is driven by the amount of InAs coverage.

Three ranges of coverage have been identified, based on electrical, structural and optical characterization.

For coverage up to 1.9 ML, the population of QDs is represented by coherent islands with a rapidly increasing density and size. This increment is responsible for the raising of accumulation peak in C-V profiles and for the increasing of the PL integrated intensity. In samples with coverage within this range, deep traps are observed in the QDs region. Their activation energy are 0.56 eV with a capture cross section of 2.7×10^{-15} cm^2, and 0.76 eV with a capture cross section of 4.5×10^{-14} cm^2. These traps have been related to deep levels already reported in the literature for InAs/GaAs QD structures, and attributed to point-defect-oxygen complexes and EL2 family, typical of bulk GaAs.

A second coverage range goes from 1.9 ML to 2.4 ML. Here, the QDs density is almost stable and only slightly increasing, with a mean value of 2×10^{11} cm^{-2}. Their size has the same trend with mean base diameters and heights reaching values around 15 an 2.2 nm, respectively. The C-V profiles show an accumulation peak with the same slight increase and the integrated PL measurements show no significant variation. DLTS traps remain the same as below 1.9ML.

The third and last explored coverage range is above 2.4 ML, where we encounter two populations of 3D islands. The first represented by coherent QD whose dimension and density remain almost unaffected by the coverage increasing, up to our maximal explored coverage of 2.9 ML. The second distribution of islands is composed of larger QDs whose density increases by an order of magnitude from 2×10^8 to 1.5×10^9 cm^{-2}. The size of those larger islands, as explained in Ref. 21 and confirmed by AFM measurements, continues to increase with coverage. The presence of this second population of islands is symptomatic of a ripening phenomenon. C-V profiles are dramatically changing in this coverage range, showing an increasing depletion of free carriers centred on the upper confining

layer. Such depletion has been attributed to acceptor-like electron levels produced by extended defects. The presence of such defects has been confirmed by DLTS analysis, from which, the evidence of deep traps related to extended defects has been provided. The activation energies of those traps are 0.52 eV with a cross section of 2.5×10^{-14} cm^2 and 0.84 eV with a cross section of 2.7×10^{-13} cm^2. The latter was found in the region around the QDs plane. We believe that those traps are responsible from the carrier depletion. Both levels showed the typical logarithmic amplitude dependence with the pulse width, indicating their correlation with extended defects. The presence of the latter have been confirmed also by TEM analysis which shows that V-shaped threading dislocations originate at those larger islands and propagate from the QD/GaAs interface through the cap layer, reaching a maximum density halfway to the surface due to a self-annihilation mechanism. Moreover, planar TEM images, show that a fraction of these larger islands plastically relax, becoming incoherent, as a consequence of their increasing size. This fraction reaches the 100% with increasing coverage. Last, the deep levels presence and their detrimental effect have been confirmed also by the integrated PL, in which is showed that the radiative recombination efficiency is considerably reduced for such high coverage.

It worth noting that the dynamics of strain accumulation and relaxation has been explained in the framework of a previous theoretical study (Ref. 35) which starts from thermodynamic principles, independent from the materials used. In this work the authors explain the phase transitions identified with two critical coverage values, the first, in our case 1.6 ML, for the 2D/3D growth mode transition and the second, in our sample singled out at about 2.4 ML, for the appearance of larger islands. This makes our work an experimental confirmation of such study, but, more important, this generality makes possible to apply those results in our future studies, for the development of improved design criteria to reach the final goal of realization of structures with QD emission wavelength in the windows of photonics interest.

Moreover, a first procedure for sample preparation and preliminary results of the implementation of Scanning Capacitance Microscopy on InAs/GaAs has been presented. The ageing of the SCM sample with exposition time to atmosphere has been evidenced.

ACKNOWLEDGEMENTS

Thank to all the people that have worked on the subject of this thesis:
Lucia Nasi of the electron microscopy group, Claudio Bocchi for X-ray measurements, Giovanna Trevisi, Luca Seravalli, Paola Frigieri and Secondo Franchi of the MBE group.
Special thank go to my supervisors Enos Gombia and. Roberto Mosca for their patience, and their efforts for make me understand electrical characterization techniques, I know it has been an hard work! (and not so fruitful….)
I want to say thanks also to Julio Cesar Rimada Herrera, for his helps in correcting the manuscript and also for the rum…

Special thank goes to my parents too.

In the end I want to say thanks to two special persons:

Grazie Francescaelisa

Grazie Graziella.

BIBLIOGRAPHY

[1] T.H. Maiman, *Nature,* (1960) **187,** 493

[2] R.N. Hall, G.E. Fenner, J. D. Kingsley, T. J. Soltys and R. O. Carlson, *Phys. Rev. Lett*. (1963) **9**, 366

[3] M. Nathan, P. Dumke, G. Burns, F. Dill and G. Lasher, *Appl. Phys. Lett*. (1962) **1**, 62

[4] T. Quist, R. Rediker, R. Keyes, W. krag, B. Lax, A. McWhorter, H. Zeigler, *Appl. Phys. Lett*. (1962) **1**, 91

[5] M. Asada, Y. Miyamoto and Y. Suematsu, *J.Quantum Elect*. (1986) **22**, 1915

[6] Arakawa and H. Sakaki.,*App. Phys. Let*. (1982) **40**, 939

[7] R. Sellin, C. Ribbat, M. Grundmann, N. Ledentsov, D. Bimberg, *Appl. Phys. Lett*. (2001) **78**, 1207

[8] F.Briones and A. Ruiz, *J. Crystal Growth*, (1991), **111**, 194

[9] I.N. Stranski and L. Krastanow, *Sitzungberichte der AdW Wien, Math. naturwiss. Klasse Abt. IIb,* (1938), **146**, 797

[10] F.C. Frank and J.H. van der Merwe, *Proc. Roy. Soc. London A*, (1949), **198**, 205

[11] M. Volmer, A. Weber, *Z. Phys. Chem*, (1926), **119**, 277

[12] L. Goldstein, F. glas, J. Marzin, M. Charasse and G. Le Roux, *Appl. Phys. Lett*, (1985), **47**, 1099

[13] D. Vanderbilt and L.K. Wickham, *Proc. Mater. Res. Soc. Symp.,* (1991), **202**, 555

[14] P. Blood and J. Orton, "The Electrical Characterization of semiconductors: majority carriers and electron states", Academic Press

[15] S.A. Ringel, *Solid State Electr.* (1997), **3**, 359

[16] T.Wosinki, *J. Appl. Phys.,* (1989), **65**, 1566

[17] T. Figielski, *Solid-State Electron.,* (1978), **21**, 1403

[18] W.T. Read, *Philos. Mag.,* (1954), **45**, 775

[19] S.M. Sze, "*physics of Semiconductor Devices*", Wiley interscience

[20] J.Matey and J. Blanc, *J. Appl. Phys.* **57** (1985) 1437

[21] C. Bugg, P. King . *J. Phys. E* **21** (1998),147

[22] H. Kleinknecht, J. Sandercock ,H. Meier, *Scanning Microsc.* **2** (1998), 1839

[23] CC. Williams, W. Hough, S. Rishton *Appl. Phys. Lett.* **55** (1989),203

[24] CC.Williams and LJ. Klein, *Rev. Sci. Instrum.* **75** (2004), 422

[25] F. Giannazzo, D. Goghero and V. Raineri, *J. Vac. Sci. Technol. B*, **22** (2004), 2391

[26] J. F. Marchiando, J. J. Kopanski and J. R. Lowney, *J. Vac. Technol. B*, **16** (1998), 463

[27] E. Nicollian and A. Goetzberger,*IEEE Trans. Electron. Devices*, **ED-12** (1965), 108

[28] C.Bocchi and C.Ferrari, *J. Phys. D*, (1995) **28**, A164

[29] M. Colocci, F. Bogani, L. Carraresi, R. Mattolini, A. Bosacchi, S. Franchi, P. Frigeri, M. Rosa-Clot, and S. Taddei, *Appl. Phys. Lett.* **70** (1997)., 3140

[30] M. J. da Silva, A. A. Quivy, P. P. González-Borrero, E. Marega, Jr., and J. R. Leite, J. Cryst. Growth **241** (2002)., 19

[31] J. B. Wang, F. Lu, S. Zhang, D. Wong, H. Sun and X. Wang, *phys. Rev. B*,(1996) **54**, 7979

[32] C.R. Moon, B. Choe, S. Kwon, H. Lim, *Appl. Phys. Lett.,* (1998), **72**, 1196

[33] E. Gombia, R. Mosca, S. Franchi, S. Frigieri, P. Ghezzi, *Mater. Sci. Eng. C*, (2006), **26**, 867

[34] M. Richter, D. Reuter, J. Duboz, A. Wieck, Physica E, (2007) *In Press*

[35] I. Daruka, J.Tersoff, A.L. Barabàsi, *Phys Rev Lett*, (1999), **82**, 2753

[36] P. Frigieri, L. Nasi, M. Prezioso, L. Seravalli, G. Trevisi, E. Gombia, R. Mosca, F. Germini, C. Bocchi and S. Franchi, *J. Appl. Phys.* (2007), **102**, 083506

[37] E. Gombia, R. Mosca, P. Frigeri, S. Franchi, S. Amighetti, and C. Ghezzi, *Mater. Sci. Eng. B*, **91**(2002), 393

[38] J. F. Chen, R. S. Hsiao, Y. P. Chen, J. S. Wang, and J. Y. Chi, *Appl. Phys. Lett.* **87** (2005)., 141911

[39] M. Kaniewska, O. Engström, A. Barcz, and M. Pacholak-Cybulska, *Mater. Sci. Eng. C* **26** (2006), 871

[40] M. Kaniewska, O. Engström, A. Barcz, and M. Pacholak-Cybulska, *Mater. Sci. Semicond. Process*. **9** (2006), 36

[41] A. Hida, Y. Mera, K. Maeda, *Physica B.* **340** (2003), 299

[42] W.R. Buchwald, M.N. Jhonson, *J. Appl. Phys*. **64** (1988), 958

[43] S. Mahajan, *Acta Mater.* **48** (2000), 137

[44] I. Daruka and L. Barabàsi, *Phys. Rev. Lett*. **79** (1997), 3708

[45] N. Wang, I. SOu and K. K. Fung, *J. Appl. Phys*. (1996), **80**, 5506

[46] K.K. Fung , N. Wang and I. Sou, *Appl. Phys. Lett.,* (1997), **71**, 1225

[47] N. Wang, K.K. Fung and I. Sou, *Appl. Phys. Lett.* (2000), **77**, 2846

[48] R. Kobayashi, T. Nakayama, *J. Cryst. Growth.* (2005), **278**, 500

[49] D. Hull and D.J.Bacon, “introduction to Dislocations”, IV edition 2005, p. 98, BH edition

[50] H.Joe, T. Akiyama, K. Nakamura, K. Kanisawa, T. Ito, *J. Cryst Growth* **301–302** (2007), 837–840

[51] K. Kanisawa, M. Butcher, Y. Tokura, H. Yamaguchi and Y. Hirayama, *Phys. Rev. Lett.* **87** (2001),196804.

[52] H.L. Hartnagel and R. Riemenschneider, *Properties of Gallium Arsenide (3rd Edition)*. (pp. 471).Edited by M.R.Brozel and G.E. Stillman